

## Mass asymmetry dependence of scission times in the reactions of 18.5 A MeV $^{136}\text{Xe} + ^{48}\text{Ti}$

M. Gui, K. Hagel, R. Wada, Y. Lou, D. Utley, B. Xiao, J. Li, and J. B. Natowitz  
*Cyclotron Institute, Texas A&M University, College Station, Texas 77843*

G. Enders, W. Kühn, V. Metag, R. Novotny, and O. Schwalb  
*II Physikalisches Institut, Universität Giessen, D-6300 Giessen, Germany*

R. J. Charity,\* R. Freifelder,<sup>†</sup> A. Gobbi, W. Henning,<sup>‡</sup> K. D. Hildenbrand, R. Mayer,  
 R. S. Simon, and J. P. Wessels<sup>§</sup>  
*Gesellschaft für Schwerionenforschung, Planck Strasse 1, D-6100 Darmstadt, Germany*

G. Casini, A. Olmi, and A. A. Stefanini  
*Università di Firenze and Istituto Nazionale di Fisica Nucleare, Florence, Italy*  
 (Received 24 May 1993)

The multiplicities of  $p$  and  $\alpha$  particles detected in coincidence with fragments emitted in fully relaxed collisions in the reactions of 18.5 A MeV  $^{136}\text{Xe} + ^{48}\text{Ti}$  have been measured for different exit channel mass asymmetries. A kinematic source analysis of the spectra and angular distributions of the light particles has been used to separate the total multiplicities into pre-scission and post-scission contributions. From these results, the excitation energies at scission are determined using an empirical technique based upon previous measurements of light charged particle multiplicities observed in coincidence with evaporation residues. These excitation energies are found to decrease from  $\sim 400$  MeV to 110 MeV as the fragment mass asymmetry,  $A_H/A_L$ , varies from 4.8 to 1.0. A corresponding increase of the mean lifetime of the scissioning nucleus from  $\sim 5 \times 10^{-22}$  s to  $\sim 1 \times 10^{-20}$  s is derived using calculated statistical model decay widths. The extent to which this variation of lifetime with mass asymmetry may be attributed to completely damped deep inelastic collisions or to dynamic delays in the decay of a compound nucleus is discussed as is the need for inclusion of dynamics in the deexcitation calculations for hot nuclei. Observed three fragment events are also discussed.

PACS number(s): 25.70.Lm, 25.70.Gh

### I. INTRODUCTION

While the deexcitation of excited equilibrated nuclei is normally treated as a statistical process, a number of experiments have provided evidence for significant departures from purely statistical descriptions, particularly in the competition between the emission of light particles and fission [1]. Dynamic delays in the fission or quasifission process have been observed to lead to pre-scission particle emission multiplicities well above those calculated from phase-space considerations alone [1–4]. Corresponding increases in residue cross sections, reflecting the decreased fission probability which results if the light particles remove significant angular momentum from the system, have also been measured [5–7]. While symmetric fission is now well established as a cold process, there is evidence that more asymmetric breakups

occur earlier in the deexcitation chain [2,8–10]. The extent to which these observations primarily reflect entrance channel deep-inelastic reaction dynamics is not clear, and a complete quantitative understanding of the dynamic hindrance as a function of exit channel mass asymmetry has not yet been developed. In this work, we have attempted to provide further information on this very interesting question by exploring the time scale of fragment emission from nuclei with  $A \simeq 180$  at excitation energies near 3 MeV/nucleon.

### II. EXPERIMENTAL TECHNIQUES

The primary object of this research was to derive the time scale of binary-fragmentation processes as a function of fragment mass asymmetry from measurements of the associated light charged particle emission. The experiment was performed at the GSI UNILAC accelerator in Darmstadt, Germany. A beam of 18.5 A MeV  $^{136}\text{Xe}^{21+}$  projectiles irradiated a self-supporting  $^{48}\text{Ti}$  target 175  $\mu\text{g}/\text{cm}^2$  thick.

Figure 1(a) shows the experimental setup. Fragments were detected in twelve large area position sensitive parallel plate avalanche counters (PPAC) [11]. These PPAC's, each 30 cm  $\times$  30 cm, were arranged in three groups and mounted in an axially symmetric configuration around the beam axis. We labeled these

\*Present address: Department of Chemistry, Washington University, St. Louis, MO 63130.

<sup>†</sup>Present address: Hospital of the University of Pennsylvania, Nuclear Instrumentation, Philadelphia, PA 19104.

<sup>‡</sup>Present address: Physics Division, Argonne National Laboratory, Argonne, IL 60439.

<sup>§</sup>Present address: Department of Physics, SUNY, Stony Brook, NY 11790.

twelve PPAC's as shown in the figure. The distance from the target to the center of each detector in the closest group of PPAC's was 30 cm, and to the farthest group was 140 cm. The fragment masses for coincident fragments were determined from the measured velocities and angles by means of a kinematic reconstruction method [12,13].

Coincident light charged particles were detected and their velocities and energies were measured using both a position sensitive plastic scintillator detector (NE102A) and a Si-CsI telescope. The plastic scintillator detector was located 1 cm behind PPAC's 1 and 2, at an angle  $\theta=9^\circ$  relative to the beam axis. The Si-CsI telescope was located at  $\theta=40^\circ$  relative to the beam, in front of PPAC 3. The distance from the telescope to the target was 39.3 cm.

The 12 parallel plate avalanche counters covered about 75% of the solid angle in the forward hemisphere. For our reversed kinematics system, this corresponded to

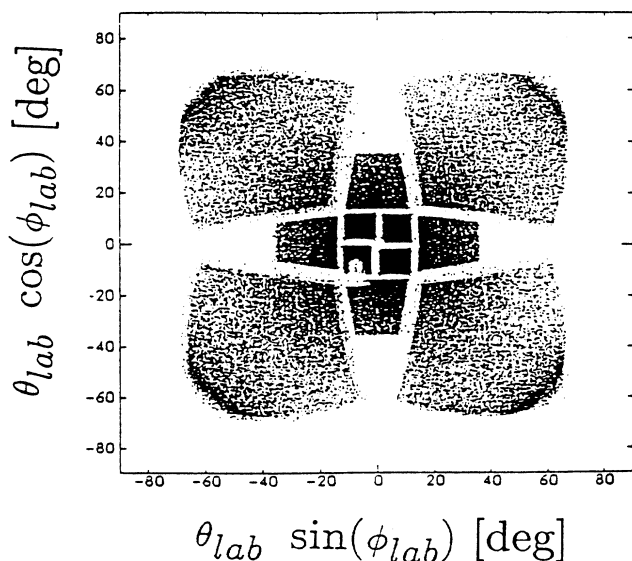
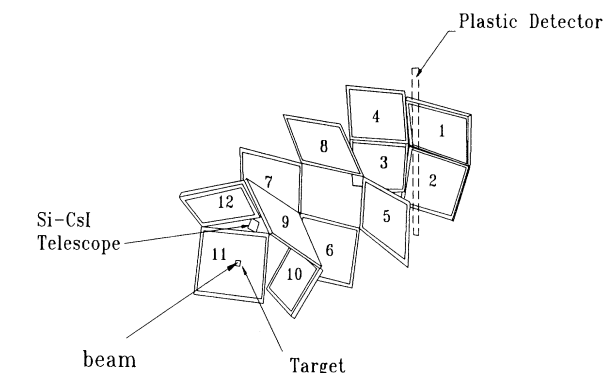


FIG. 1. (a) Experimental setup. Twelve PPAC's are arranged concentric to the beam in the forward hemisphere. (b) Projections of the fragment positions measured in the PPAC's onto a plane perpendicular to the beam.

nearly  $4\pi$  in the center-of-mass frame. Figure 1(b) shows a projection of the observed fragment positions onto the plane perpendicular to the beam axis. This figure demonstrates the large geometric efficiency of the detectors for the reaction  $18.5 A \text{ MeV } ^{136}\text{Xe} + ^{48}\text{Ti}$ .

In order to determine the velocity of a heavy fragment, both the flight path and the flight time were measured. The spatial positions of the PPAC's were determined by measuring the distances from the target to three reference points on each detector using a laser beam which was placed on a rotating table. The time calibrations of the detectors were performed using the elastic scattering of 5.9 MeV/nucleon  $^{120}\text{Sn}$  ions from a  $^{197}\text{Au}$  target. The overall time resolution was 1 ns. The position resolution was 3 mm. From the measured position and time information, the experimental velocity vectors of the detected fragments were determined.

The detection efficiency of the PPAC is dependent on the energy loss in the PPAC and the discriminator threshold [14,15]. For small nuclear charge, only low-energy ions can be detected. As  $Z$  increases,  $V_{max}$ , the maximum velocity at which an ion can be detected, increases. For  $Z \leq 5$ , the detector efficiency is very small; for  $Z \approx 10$ , the efficiency is 80%, and for  $Z \geq 15$ , the efficiency is nearly 100% in our experiment.

#### A. Light charged particle detection

The thickness of the plastic scintillator was 1 cm. It was 5 cm wide and 100 cm long. Photomultiplier tubes were attached to both ends of the scintillator. In order to increase the light output and prevent light peaks, the scintillator was wrapped with  $4 \text{ mg/cm}^2$  aluminum foil. For particles incident on the plastic scintillator, the flight time was determined and the position obtained from a measurement of the time difference  $\Delta t$  for signals at the two ends.

The apparent energy,  $E_0$ , deposited in the scintillator of length  $l$  can be related to the energy signals observed by the photomultiplier tubes at each end:

$$E_1 = E_0 \exp(-\lambda X_0), \quad (1)$$

$$E_2 = E_0 \exp[-\lambda(l - X_0)], \quad (2)$$

where  $\lambda$  is the attenuation length and  $X_0$  is the distance from one end. Multiplying  $E_1$  by  $E_2$ , and taking the square root, we obtain the apparent deposited energy

$$E_0 = \sqrt{E_1 E_2} \exp(\lambda l), \quad (3)$$

which is independent of the position  $X_0$ .

Particle mass identification was accomplished from observations of apparent energy  $E_0$  versus time of flight  $t$ . Taking advantage of this particle identification, we determined the actual light charged particle energies from the measured particle velocities  $v$  and known proton and  $\alpha$ -particle masses.

The Si-CsI telescope consisted of a  $25 \mu\text{m}$  silicon detector followed by a  $300\text{-}\mu\text{m}$ -thick silicon detector and a 1-cm-thick CsI detector. Because of the positioning of this telescope, the light charged particles with velocities in the center of mass frame below 2.8 cm/ns were not

detected. This detector still served as a useful tool to verify the results obtained from the plastic scintillator detector.

### B. Kinematic reconstruction

We used a previously developed kinematic coincidence method to reconstruct the primary fragment masses [12,13]. For each detected fragment, the velocity vector  $v_{\text{exp}}$  was determined from the measured time of flight and the position coordinates in the PPAC. Even when corrected for resolution and energy loss in the target, the measured fragment velocity vectors differ from the primary ones as a result of perturbations from the emission of light particles. The essential hypothesis of the kinematic reconstruction method is that light particles are isotropically emitted from the fragments. The method is applied in a self-consistent way to the evaluation of binary and ternary events by determining the primary masses to fulfill the kinematic requirements with minimal readjustment of the experimental velocities. This is achieved in a least-squares procedure by minimizing the expression

$$\Delta_v^2 = \sum_{i=1}^n |(v_i^{\text{exp}} - v_i)|^2 \quad (4)$$

under the constraints of mass and momentum conservation

$$\sum_{i=1}^n m_i v_i = \mathbf{0} , \quad (5)$$

$$\sum_{i=1}^n m_i = m_{\text{tot}} , \quad (6)$$

with  $n=2$  for two-body events and  $n=3$  for three-body events. This system of equations was solved in an iterative procedure using the measured experimental velocities as starting values.

### C. Characterization of the system

The system we have investigated is  $^{136}\text{Xe} + ^{48}\text{Ti}$ . The incident energy was 18.5 MeV/nucleon. The beam velocity was 5.97 cm/ns. The center-of-mass velocity is 4.42 cm/ns.

The grazing angle  $\theta_{\text{gr}}^{\text{c.m.}}$  in the center of mass is  $12.4^\circ$  and in the laboratory frame is  $3.2^\circ$ . The grazing angular momentum is  $367\hbar$ . The most probable total kinetic energy for the fission fragments, calculated from Viola systematics [16], would be 128 MeV. If a compound nucleus is formed, the initial excitation energy of the compound nucleus  $^{184}_{76}\text{Os}$  calculated for 100% linear momentum transfer would be 574 MeV or 3.12 MeV/nucleon.

## III. EXPERIMENTAL RESULTS

### A. Fragment mass and TKE

Figure 2(a) contains a contour plot of total kinetic energy (TKE) versus primary fragment mass  $A$  for the binary events in the 18.5 MeV  $^{136}\text{Xe} + ^{48}\text{Ti}$  system. In

our subsequent analysis, we have focused on events with high total kinetic-energy loss leading to products falling within the window indicated by the dashed lines in this figure. The fragment mass distribution for products in this damped collision window is shown in Fig. 2(b). In order to study the precission time scale as a function of fission fragment mass asymmetry, we have selected four mass asymmetry bins. The four mass asymmetry regions selected were  $A_H/A_L = (1-1.24)$ ,  $(1.24-1.97)$ ,  $(1.97-3.38)$ , and  $(3.38-7.36)$ . We call these four windows: Asy1, Asy2, Asy3, and Asy4. The first case, Asy1, corresponds to symmetric breakup, and the last, Asy4, corresponds to the most asymmetric breakup.

To evaluate the linear momentum transfer in our sys-

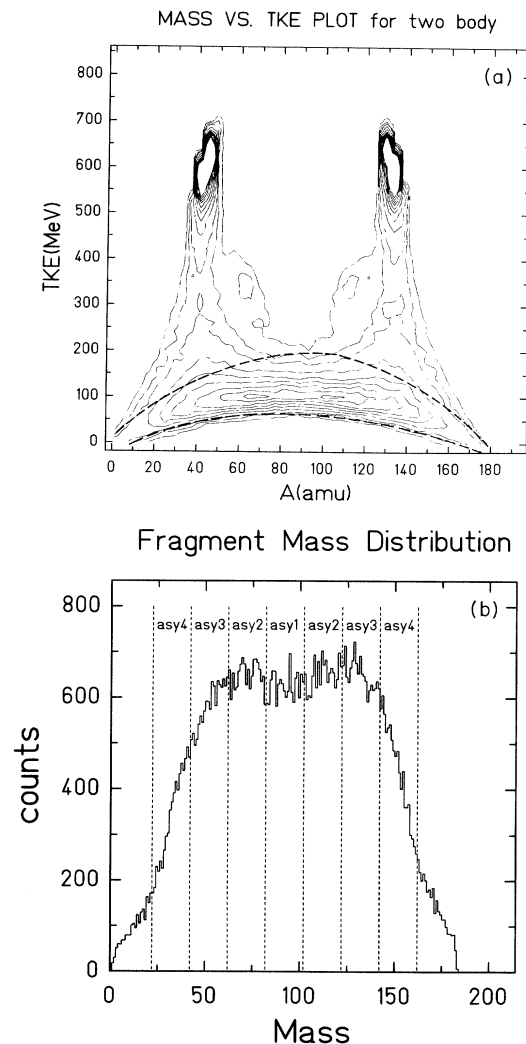


FIG. 2. (a) Contour plot of the differential cross section  $d^2\sigma/dTKE dA$  for detected twofold events as a function of the primary mass ( $A$ ). The outermost contour in the contour plot is 100 events, the next is 300, the third is 500, then contours increase linearly by increments of 500. The total primary fragment mass is  $A_{\text{tot}} = 184$ . (b) Mass distribution of the relaxed events selected for this analysis. The four asymmetry windows are indicated.

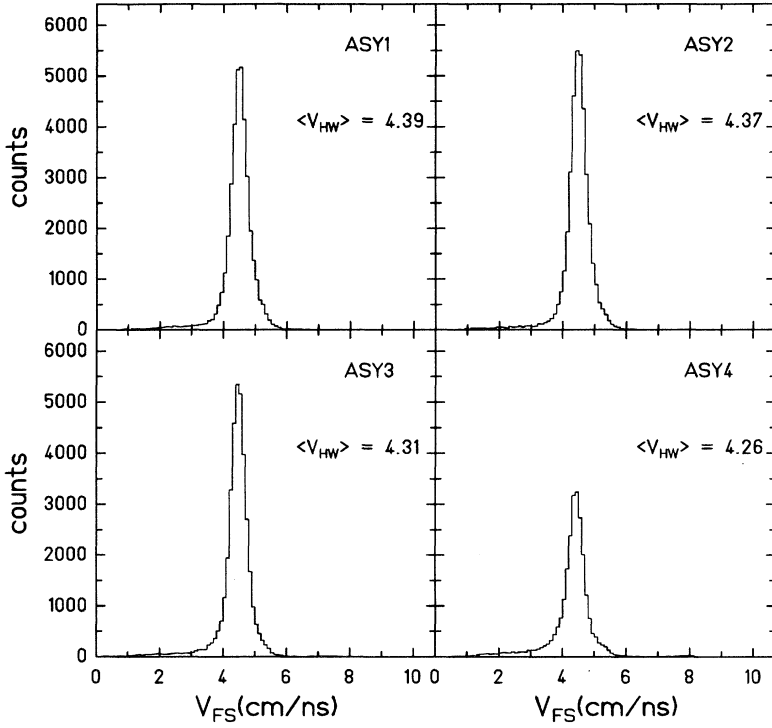


FIG. 3. Velocities of the fissioning frame for the four mass asymmetry windows, where  $\langle V_{HW} \rangle$  is the velocity averaged over the half-width of the velocity spectrum.

tem, we used the measured fragment velocity vectors to extract the velocity of the fissioning system  $v_{FS}$ . If  $v_1$  and  $v_2$ , respectively, are the velocities of the heavier and lighter fragments and  $\theta'$  is the angle of the relative velocity vector in the center-of-mass frame, then

$$\mathbf{v}_{rel} = \mathbf{v}_H - \mathbf{v}_L, \quad (7)$$

$$\theta' = \arccos(\mathbf{v}_{rel} \cdot \mathbf{Z}_0 / v_{rel}). \quad (8)$$

Here  $\mathbf{Z}_0$  is a unit vector on the  $Z$  axis which is chosen to lie in the direction of the beam. The velocity of the scissioning system is then

$$v_{FS} = v_H \cos \theta_1 - v_L \sin \theta_1 \cot \theta'. \quad (9)$$

Figure 3 shows the  $v_{FS}$  distributions for the four mass asymmetry windows. For the very central collisions selected here, the mean velocities we derive are very close to, but slightly lower than, the calculated c.m. velocity of 4.42 cm/ns. The largest apparent deviation of 4% is observed for the most asymmetric window Asy4. Assuming no systematic error in the evaluation, the results suggest a slightly greater mass loss from the projectile than from the target nucleus.

### B. Particle spectra

To analyze the particle spectra, we have used the relative velocity vectors of the two fragments to determine the orientation of the scission axis  $F$ . We then define a frame, which we call the scission frame, in which particle emission angles are measured relative to the scission axis (Fig. 4). In the scission frame, by definition, the heavier fragment is emitted at  $0^\circ$  and the lighter fragment at  $180^\circ$ , and the angle between an  $\alpha$  particle or proton and the

scission axis is  $\theta_s$ . The angle  $\theta_s$  may be calculated from the relative velocity vector of the two fragments  $v_{rel}$  and the coincident light particle velocity vector  $v_\alpha$ ,

$$\theta_f = \arccos(\mathbf{v}_{rel} \cdot \mathbf{v}_\alpha / v_{rel} v_\alpha). \quad (10)$$

The energy distribution of emitted light charged particles in the source rest frame may be represented as

$$\frac{d^2\sigma}{d\Omega d\epsilon} = \frac{N(\epsilon - E_C)}{4\pi T^2} \exp\left[\frac{-(\epsilon - E_C)}{T}\right], \quad (11)$$

where  $T$  is the source temperature,  $\epsilon$  is the particle energy, and  $E_C$  is the Coulomb energy of the particle. The emitted light particle energy distribution from the fragment source may be transformed into the center-of-mass frame using the relationship

$$\left[\frac{d^2\sigma}{d\Omega dE}\right]_{c.m.} = \left[\frac{E_{c.m.}}{E'}\right]^{1/2} \left[\frac{d^2\sigma}{d\Omega dE}\right]_{E=E'}. \quad (12)$$

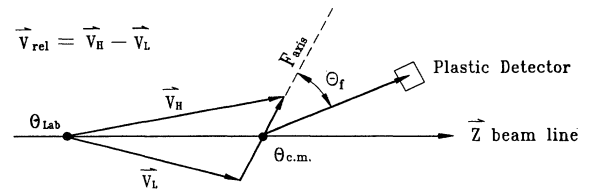


FIG. 4. Sketch of a typical twofold event with a light particle in coincidence; definition of the fission axis  $F$ . Particle emission angles are measured relative to this axis.

Here  $E_{c.m.}$  is the energy in the center of mass and  $\theta_{c.m.}$  is the angle in the c.m. frame,

$$E' = E_{c.m.} + E_s - 2(E_{c.m.} E_s)^{1/2} \cos(\theta_{c.m.} - \theta_s),$$

$E_s$  is the energy of a particle moving with the source velocity, and  $\theta_s$  is the angle of the source velocity vector in the center-of-mass frame. We have constructed  $\alpha$  and proton center of mass energy spectra at different  $\theta_f$  relative to the fission axis. In that way we could use all the events in which fragments were coincident with light particles detected in the plastic detector, thus taking full advantage of the  $4\pi$  detector to obtain good counting statistics.

For the determination of light particle multiplicities,

the experimental energy spectra of light particles observed in coincidence with two fission fragments have been fit with a moving source model in which the particles are assumed to be emitted isotropically from three moving sources, one corresponding to the compound nucleus, and the other two corresponding to the two fission fragments. For each mass asymmetry window, we determine both pre-scission and post-scission  $\alpha$  and proton multiplicities from those fits as discussed in the following.

### C. Galilean invariant velocity distributions

To get an overall view of the particle emission in the scission frame, we have constructed Galilean invariant velocity distributions. In Figs. 5(a)–5(d), the  $\alpha$ -particle

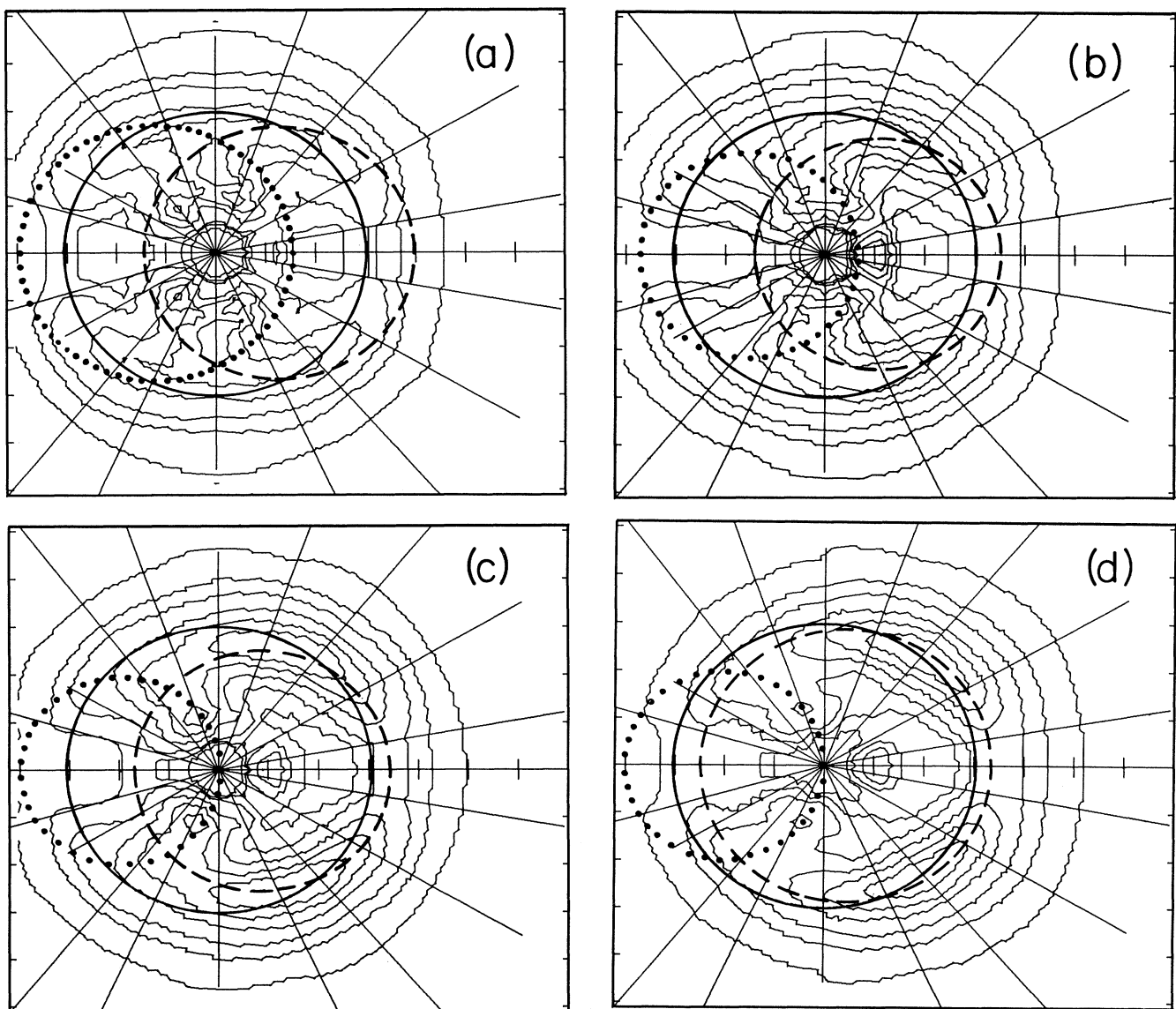


FIG. 5. Galilean invariant plots. (a) for Asy1, (b) for Asy2, (c) for Asy3, and (d) for Asy4. The solid circles in these figures show the most probable velocities for  $\alpha$  particles evaporated from the composite system, while the dashed circles represent the most probable velocities for  $\alpha$  particles emitted from the heavier fragments, and the dotted circles represent the most probable velocities for  $\alpha$  particles emitted from the lighter fragments.

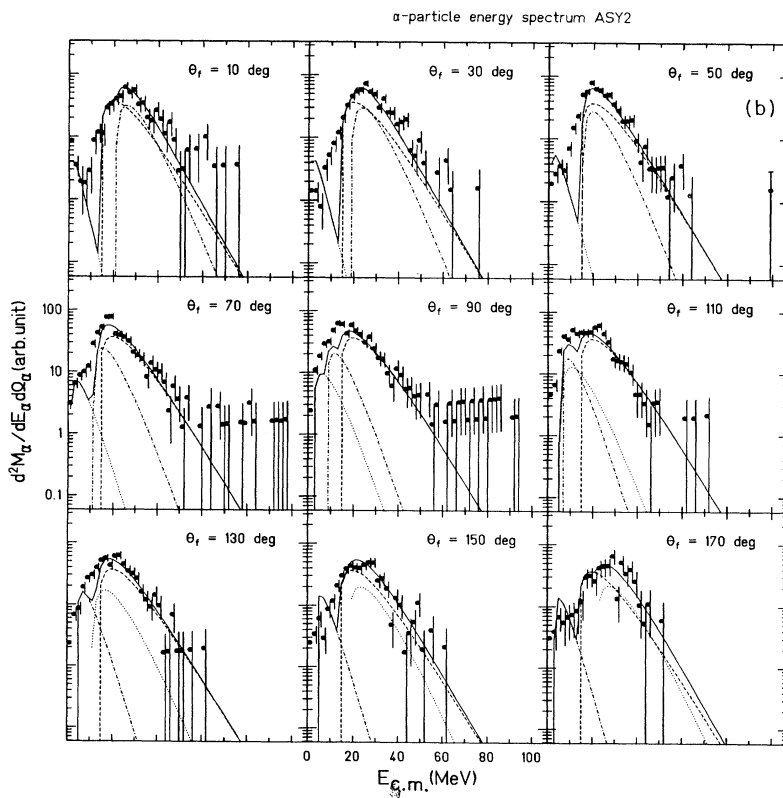
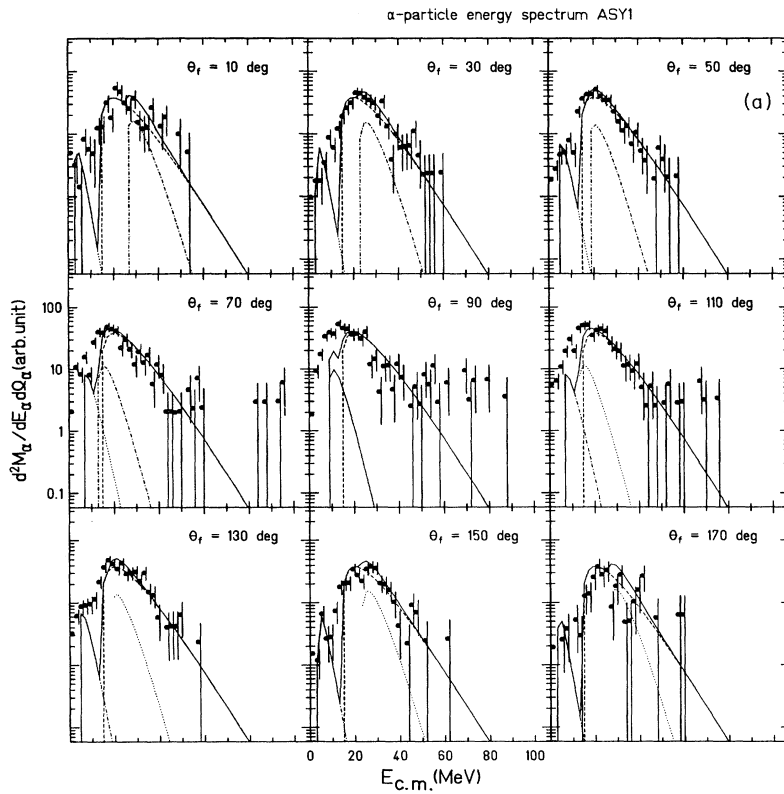


FIG. 6. (a)–(d) The energy spectra of  $\alpha$  particles observed in coincidence with fission fragments and the fit results for the four mass asymmetry windows. The solid dots with error bars represent the experimental results. The lines represent the results from the fits. Dashed lines represent the emission from the composite system prior to scission (pre-scission  $\alpha$  particles). The dot-dashed lines represent the contribution from the heavier fragments, and the dotted lines represent the contribution from the lighter fragments (post-scission  $\alpha$  particles). The solid lines show the sum of these three contributions.

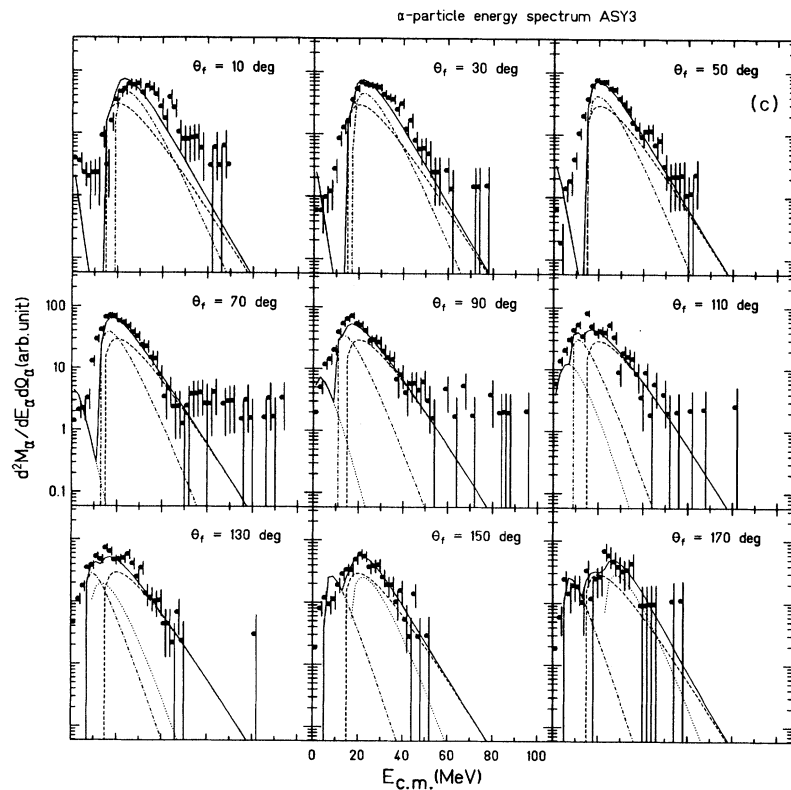
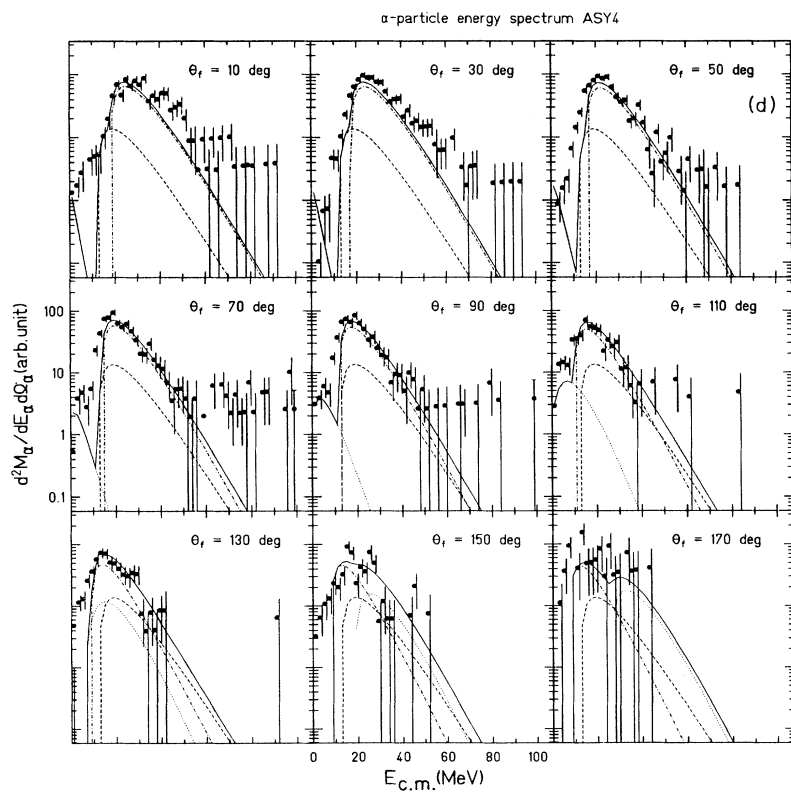


FIG. 6. (Continued).



velocity distributions are presented as contour plots for  $\alpha$  particles detected in coincidence with the fission fragments for the four different mass asymmetry windows. Recall that in the scission frame the heavier fragment moves at  $0^\circ$ , the lighter fragment moves at  $180^\circ$ , and the compound nucleus source velocity is 0. The solid circles in the figures show the most probable velocities for  $\alpha$  particles evaporated from the composite system, while the dashed circles represent the most probable velocities for  $\alpha$  particles emitted from the heavier fragments, and the dotted circles represent the most probable velocities for  $\alpha$  particles emitted from the lighter fragments. All of these most probable velocities were determined from the source fit parameters discussed in the following section. From the velocity plots, we can see that a significant fraction of the  $\alpha$  particles are emitted from the composite system. We also note that as the mass asymmetry increases,  $\alpha$  particles emitted from the heavier fragment become increasingly important. This is consistent with an increasing excitation energy of the heavier fragment for more asymmetric mass splits.

#### D. $\alpha$ particle multiplicities

We used Eqs. (11) and (12) with experimentally determined composite system and fragment source velocities to obtain a global fit to the measured  $\alpha$  energy spectra in nine different angular increments of  $20^\circ$  ranging from  $0$  to  $180^\circ$  in the scission frame. The parameters searched in the least-squares fit were the three  $\alpha$ -particle multiplicities, apparent source “temperatures,” and Coulomb barriers. Figures 6(a)–6(d) present the energy spectra of the  $\alpha$  particles observed in coincidence with fission fragments as well as the corresponding fit spectra for the four different mass asymmetry windows. The solid dots with

$\alpha$  Multiplicities as Function of Mass Asymmetry

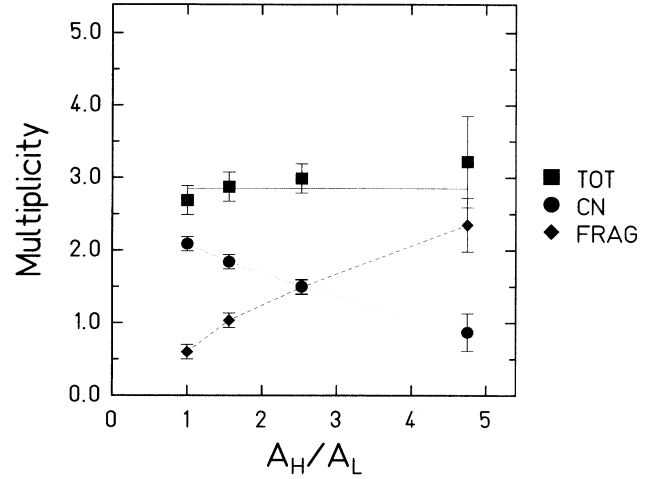


FIG. 7.  $\alpha$ -particle multiplicities extracted from the source fits. The squares indicate the total multiplicities, the dots indicate the precission  $\alpha$ -particle multiplicities, and the diamonds indicate the postscission  $\alpha$ -particle multiplicities. Lines are to guide the eye.

error bars represent the experimental data. The various curves represent the results from the fits. Dashed lines represent the fitted contribution from the composite system (precission  $\alpha$ -particle emission). The dot-dashed lines indicate the contributions from the heavier fragments, and the dotted lines show the contributions from the lighter fragments. The solid lines correspond to the sums of these three source contributions. Table I contains the fit parameters for each case. In the fitting pro-

TABLE I.  $\alpha$  emission parameters.  $A_{FH}$  is the heavier fragment mass.  $A_{FL}$  is the lighter fragment mass.  $M_{CN}$  is the  $\alpha$  multiplicity from the composite system source (precission  $\alpha$  multiplicity),  $M_{FH}$  is the  $\alpha$  multiplicity from the heavier fragment source, and  $M_{FL}$  is the  $\alpha$  multiplicity from the lighter fragment source.  $M_{frag}$  is the total  $\alpha$  multiplicity from two fragment sources (postscission  $\alpha$  multiplicity),  $M_{tot}$  is the total  $\alpha$  multiplicity from the three sources.  $T_{CN}$ ,  $T_{FH}$ , and  $T_{FL}$  are the apparent temperatures of the composite system, the heavier fragment and the lighter fragment sources, respectively,  $E_{sFH}$  and  $E_{sFL}$  are the energies of  $\alpha$  particles moving with the source velocities of the composite system, the heavier fragment and the lighter fragment sources, respectively.  $E_{bCN}$ ,  $E_{bFH}$ , and  $E_{bFL}$  are emission barriers of the composite system, heavier fragment and lighter fragment sources, respectively.

	Asy1	Asy2	Asy3	Asy4
$A_{FH}/A_{FL}$	0.8–1.24	1.24–1.97	1.97–3.38	3.38–7.36
$M_{CN}$	$2.09 \pm 0.1$	$1.84 \pm 0.1$	$1.5 \pm 0.1$	$0.87 \pm 0.26$
$T_{CN}$	$6.5 \pm 0.3$	$6.7 \pm 0.3$	$6.8 \pm 0.5$	$6.8 \pm 0.5$
$E_{bCN}$	$12.3 \pm 0.5$	$13.1 \pm 0.5$	$13.3 \pm 0.6$	$12.4 \pm 0.5$
$M_{FH}$	$0.30 \pm 0.05$	$0.66 \pm 0.04$	$1.16 \pm 0.05$	$2.1 \pm 0.3$
$T_{FH}$	$2.5 \pm 0.3$	$3.8 \pm 0.5$	$4.2 \pm 0.5$	$6.0 \pm 0.5$
$E_{sFH}$	3.0	2.1	1.2	0.6
$E_{bFH}$	$11.0 \pm 0.5$	$9.7 \pm 0.3$	$10.2 \pm 0.5$	$11.5 \pm 0.5$
$M_{FL}$	$0.30 \pm 0.05$	$0.38 \pm 0.05$	$0.33 \pm 0.05$	$0.25 \pm 0.07$
$T_{FL}$	$2.5 \pm 0.3$	$3.8 \pm 0.8$	$2.9 \pm 1.0$	$3.6 \pm 1.0$
$E_{sFL}$	3.0	4.7	6.7	8.3
$E_{bFL}$	$11.0 \pm 0.5$	$6.3 \pm 0.7$	$5.0 \pm 1.0$	$5.2 \pm 2.0$
$M_{frag}$	$0.60 \pm 0.1$	$1.04 \pm 0.09$	$1.49 \pm 0.1$	$2.35 \pm 0.37$
$M_{tot}$	$2.69 \pm 0.2$	$2.88 \pm 0.19$	$2.99 \pm 0.2$	$3.22 \pm 0.63$

cedure, isotropic angular distributions have been assumed.

Since the range of out-of-plane information is restricted in this case, we estimate that the absolute multiplicities may be in error by 20%. Similar fits to the data from the Si telescope, which covers a broader range of out-of-plane angles, are in agreement with the parameters extracted from the plastic detector data. For the purpose of extracting excitation energies at scission, only the relative multiplicities are required if the particle angular distributions do not change significantly with asymmetry window.

The variation of the  $\alpha$ -particle multiplicity with scission mass asymmetry is shown in Fig. 7. While the total  $\alpha$  multiplicities for different mass splits remain nearly constant, the prescission  $\alpha$  multiplicities decrease, and the postscission multiplicities increase with increasing mass asymmetry. The low  $\alpha$ -particle multiplicities observed for fragments from symmetric breakup indicate that the symmetric division occurs at a low excitation energy near the end of the de-excitation cascade. The decrease of the prescission  $\alpha$  multiplicity and the increase of the postscission  $\alpha$  multiplicity with increasing mass asymmetry implies that for the relaxed events analyzed, the more asymmetric the mass split, the earlier the scission occurs.

#### E. Near scission $\alpha$ -particle emission

In general, the “fit” to the particle energy spectra displayed in Figs. 6(a)–6(d) is quite good, except for the low-energy regions ( $\leq 16$  MeV) at  $\theta_s$  near  $90^\circ$  in the Asy1 and Asy2 cases. The surplus in our  $\alpha$ -energy spectra around  $\theta_s \sim 90^\circ$  appears to be the contribution of another source, in which the  $\alpha$  particles are emitted perpendicu-

lar to the scission axis. Many previous experimental results indicate the existence of  $\alpha$  particles emitted near or during scission [8,18–20]. These near-scission particles have lower energies than those evaporated from a composite nucleus, and exhibit a strong angular focusing perpendicular to the scission axis. In Fig. 6(a), we see evidence of significant near-scission-emission in symmetric breakup. As the mass asymmetry increases, the near-scission-emission is less prominent. By comparing the experimental  $\alpha$  energy spectra and the three source fit spectra at low energy, we estimate the near-scission-emission  $\alpha$  multiplicities to be  $0.3 \pm 0.1$  for the Asy1 and Asy2 windows.

#### F. Proton multiplicities

Prescission and postscission proton multiplicities were extracted using the same techniques as were used for  $\alpha$  particles. Figures 8(a)–8(d) show the experimental proton energy spectra together with the results from the three moving source fit. The solid dots with error bars show the experimental results. The curves represent the results from the fits. The dashed lines represent the spectra of protons emitted prior to scission (prescission proton emission). The dot-dashed lines indicate the contributions from the heavier fragments, and the dotted lines represent the contributions from the lighter fragments. The solid lines show the sums of the three source contributions. For protons, Table II presents the fit parameters for the three sources in the four mass asymmetry windows. The symbols used in Table II are the same as in Table I. The prescission and postscission proton emission probabilities for different fragment mass splits have very similar features to those for the  $\alpha$ -particle emission. As the mass asymmetry increases, the prescission proton

TABLE II.  $p$  emission parameters.  $A_{\text{FH}}$  is the heavier fragment mass.  $A_{\text{FL}}$  is the lighter fragment mass.  $M_{\text{CN}}$  is the proton multiplicity from the composite system source (prescission proton multiplicity),  $M_{\text{FH}}$  is the proton multiplicity from the heavier fragment source, and  $M_{\text{FL}}$  is the proton multiplicity from the lighter fragment source.  $M_{\text{frag}}$  is the total proton multiplicity from two fragment sources (postscission proton multiplicity),  $M_{\text{tot}}$  is the total proton multiplicity from the three sources.  $T_{\text{CN}}$ ,  $T_{\text{FH}}$ , and  $T_{\text{FL}}$  are the apparent temperatures of the composite system, the heavier fragment and the lighter fragment sources, respectively.  $E_{\text{sCN}}$ ,  $E_{\text{sFH}}$ , and  $E_{\text{sFL}}$  are the energies of protons moving with the source velocities of the composite system, the heavier fragment, and the lighter fragment sources, respectively.  $E_{\text{bCN}}$ ,  $E_{\text{bFH}}$ , and  $E_{\text{bFL}}$  are emission barriers of the composite system, heavier fragment, and lighter fragment sources, respectively.

	Asy1	Asy2	Asy3	Asy4
$A_{\text{FH}}/A_{\text{FL}}$	0.8–1.24	1.24–1.97	1.97–3.38	3.38–7.36
$M_{\text{CN}}$	$2.44 \pm 0.10$	$2.2 \pm 0.1$	$1.72 \pm 0.17$	$0.88 \pm 0.12$
$T_{\text{CN}}$	$4.0 \pm 0.2$	$4.0 \pm 0.2$	$4.1 \pm 0.2$	$4.2 \pm 0.2$
$E_{\text{bCN}}$	$5.3 \pm 0.4$	$5.3 \pm 0.3$	$5.2 \pm 0.5$	$5.4 \pm 0.5$
$M_{\text{FH}}$	$0.22 \pm 0.04$	$0.51 \pm 0.1$	$0.93 \pm 0.1$	$1.90 \pm 0.12$
$T_{\text{FH}}$	$2.1 \pm 0.3$	$3.0 \pm 0.3$	$3.3 \pm 0.4$	$3.5 \pm 0.4$
$E_{\text{sFH}}$	0.75	0.52	0.29	0.16
$E_{\text{bFH}}$	$3.6 \pm 0.5$	$4.0 \pm 0.5$	$4.5 \pm 0.5$	$5.0 \pm 0.5$
$M_{\text{FL}}$	$0.22 \pm 0.04$	$0.17 \pm 0.07$	$0.11 \pm 0.10$	$0.22 \pm 0.10$
$T_{\text{FL}}$	$2.1 \pm 0.3$	$2.2 \pm 0.5$	$2.5 \pm 0.7$	$2.5 \pm 1.0$
$E_{\text{sFL}}$	0.75	1.2	1.7	2.1
$E_{\text{bFL}}$	$3.6 \pm 0.5$	$3.0 \pm 1.0$	$1.7 \pm 1.0$	$2.1 \pm 1.0$
$M_{\text{frag}}$	$0.44 \pm 0.08$	$0.68 \pm 0.17$	$1.04 \pm 0.2$	$2.12 \pm 0.22$
$M_{\text{tot}}$	$2.88 \pm 0.18$	$2.88 \pm 0.27$	$2.76 \pm 0.37$	$3.00 \pm 0.34$

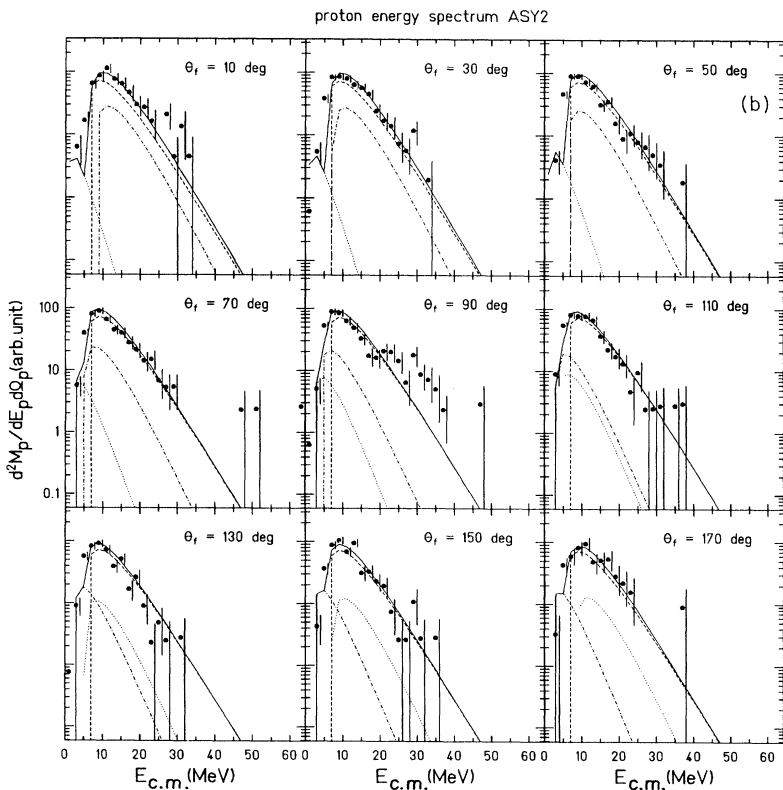
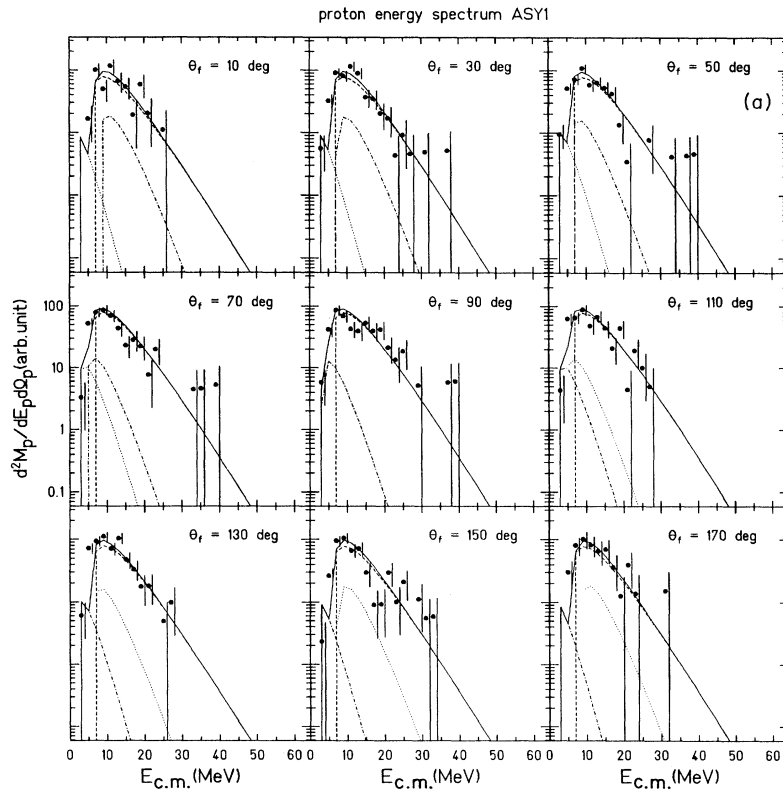


FIG. 8. (a)–(d) The energy spectra of protons observed in coincidence with fission fragments and the fit results for the four mass asymmetry windows. The solid dots with error bars represent the experimental results. The lines represent the results from the fits. Dashed lines represent the emission from the composite system prior to scission (pre-scission protons). The dot-dashed lines represent the contribution from the heavier fragments, and the dotted lines represent the contribution from the lighter fragments (post-scission protons). The solid lines show the sum of these three contributions.

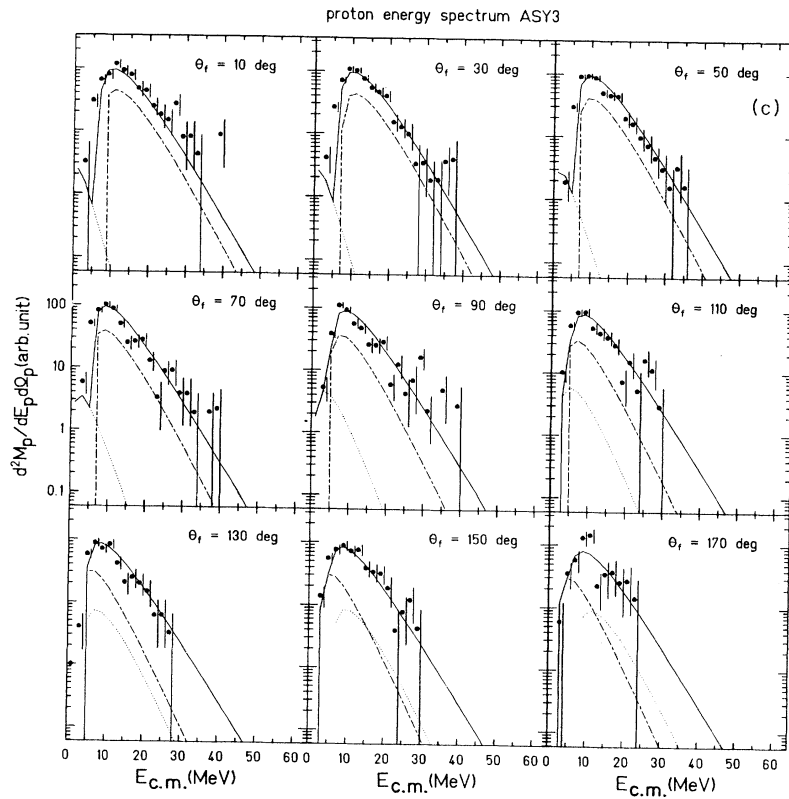
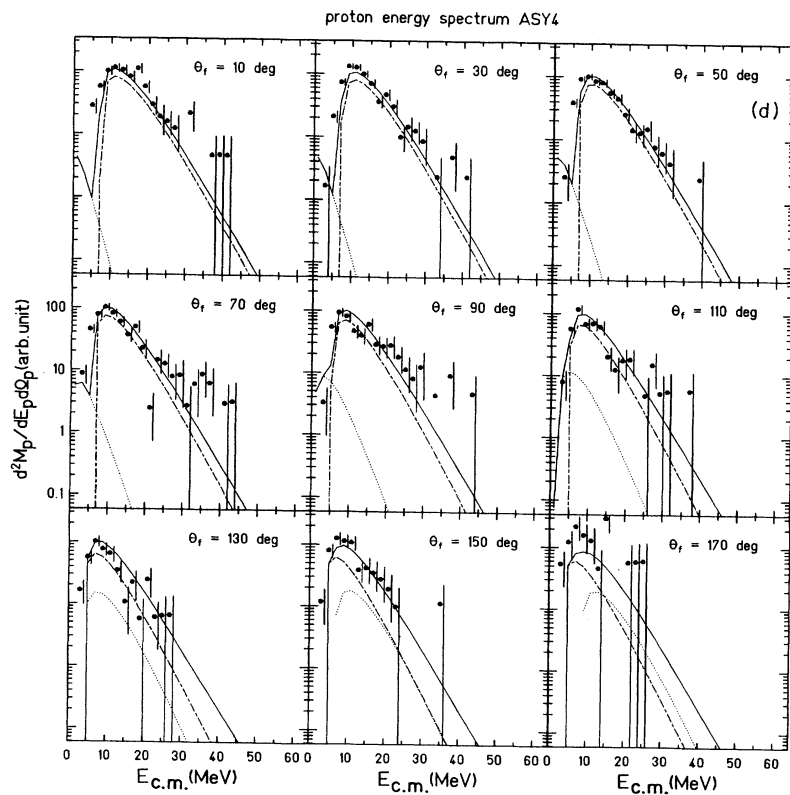


FIG. 8. (Continued).



multiplicity decreases, and the postscission proton multiplicity increases. The total proton multiplicities are similar in all cases. (See Fig. 9.)

### G. Kinematic effects of precession particle emission

In our analysis, the primary fragment masses at scission have been extracted from measured fragment velocity vectors by means of a kinematic reconstruction. In that kinematic reconstruction, we assumed that the total mass at the scission point is the sum of the projectile mass and the target mass ( $A_{\text{tot}} = A_p + A_t = 184$ ).

As we have seen in the previous section, there is significant precession particle emission. How does this affect our mass determination? For highly excited medium mass nuclei, the average excitation energy removed per unit of total evaporated mass appears to be about 15 MeV [21]. From this, and the excitation energy difference between the initial composite nucleus and the nucleus at scission (which can be determined from our study of the precession and postscission light particle emission as detailed in a later section), we estimate a 30 mass unit decrease before scission for symmetric breakup, and with increasing mass asymmetry, 25, 20, and 11 mass unit decreases for the other three cases. We have carried out kinematic reconstructions assuming masses at scission which are consistent with such precession mass losses. Figure 10 shows, as a function of  $A$ , the originally deduced mass, the mass difference  $\Delta A = (A' - A)$  where  $A'$  is the mass determined assuming precession emission. The ratio of the two fragment masses deduced before the subtraction,  $A_1/A_2$ , and after the subtraction,  $A'_1/A'_2$ , are compared in Fig. 11. The results demonstrate that when the total mass of the scissioning system is reduced, the kinematic reconstruction method reduces the extract-

P Multiplicities as Function of Mass Asymmetry

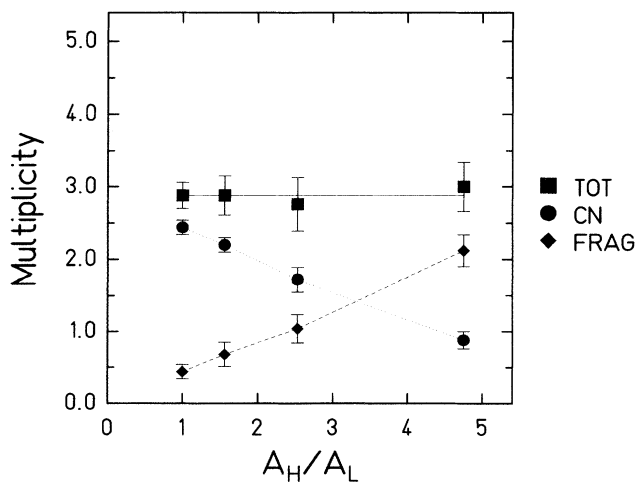


FIG. 9. Proton multiplicities extracted from the source fits. The squares indicate the total multiplicities, the dots indicate the precession proton multiplicities, and the diamonds indicate the postscission proton multiplicities. Lines are to guide the eye.

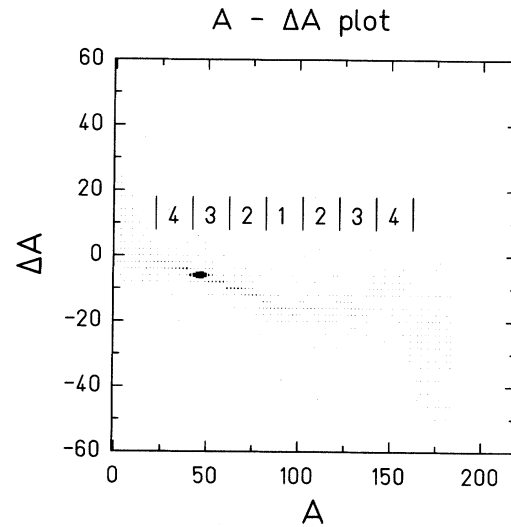


FIG. 10. Difference between the fragment mass deduced assuming  $A_{\text{tot}} = 184$  or by  $A'_{\text{tot}} = 184 - \Delta A_{\text{precession}}$   $\Delta A = A - A'$ .  $A$  is the fragment mass. The ranges corresponding to asymmetry windows 1–4 are indicated on the figure.

ed fragment masses as expected. At the same time, the fragment mass ratio does not change very much. The four fragment mass asymmetry windows we have used are essentially unchanged by the precession emission. A more extensive discussion of the effects of precession emission has been given previously by Charity *et al.* [22].

### H. Effects of three-body events

Another possible source of error in our kinematic reconstruction is contamination from incomplete detec-

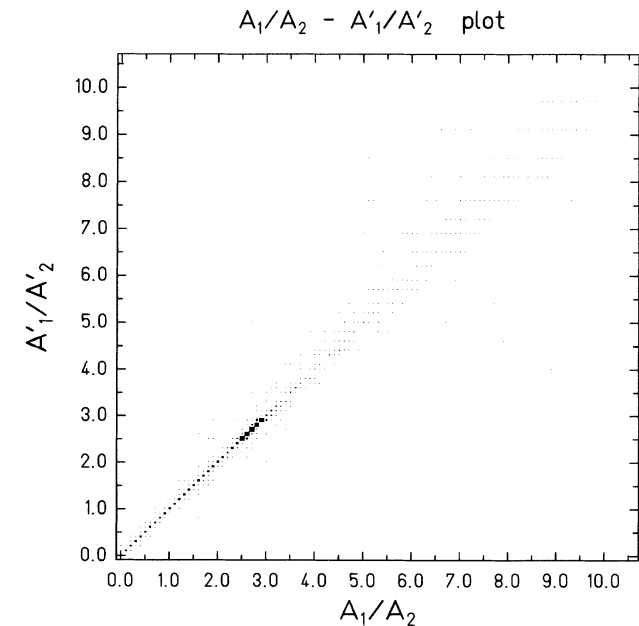


FIG. 11. Comparison between the fragment mass ratios deduced using  $A_{\text{tot}} = 184$  and  $A'_{\text{tot}} = 184 - \Delta A_{\text{precession}}$ .

tion of events with higher fragment multiplicity. In our experiment, the solid angle covered by 12 PPAC detectors is not a full  $4\pi$  sr in the center-of-mass frame. As a consequence, detected twofold coincidence events may contain not only true two-body events, but also contributes from three-body (or higher) multiplicity events in which only two fragments were detected. In addition, the intrinsic efficiency of the PPAC's is not 1. If the missing third body is sufficiently large, these incompletely detected events would be reproduced poorly by the two-body kinematic reconstruction.

In fact, we observe a significant number of events where three bodies are detected. By analyzing these events with one fragment excluded from the analysis, we have concluded that the bulk of events in which a third fragment is missed corresponds to events in which that fragment is small and has little effect on the determination of the mass asymmetry ratio of the two larger fragments. We believe that most of such events correspond to evaporation of intermediate mass fragments (IMF) prior to scission. The estimated multiplicity of such IMF's is approximately 1, but this estimate is subject to large uncertainties. The kinematic analysis which leads to these conclusions is discussed in greater detail in the Appendix as is the nature of the detected three-body events.

#### IV. INTERPRETATION OF RESULTS

##### A. Excitation energies at scission

Light particles emitted from a composite system during the deexcitation process can be used as a "clock" to yield the dynamical scission time scale [23]. The mean emission lifetime at each step in the deexcitation is given by  $\tau = \hbar/\Gamma$  where  $\Gamma$  is the total decay width at that excitation energy. The precission lifetime can be obtained by summing the mean light particle emission lifetimes over the deexcitation cascade from the initial excitation energy at which the compound nucleus was formed to the excitation energy at which the system scissions [22].

In order to deduce the precission time scales as a function of different fission fragment mass asymmetries with minimum reliance on the statistical model at high excitation energy, we have employed an empirical method to determine the excitation energies at scission. We then employed a statistical model calculation to estimate the cumulative lifetimes corresponding to the excitation energies which were derived.

##### B. Symmetric breakup

One way to deduce the excitation energy at the scission point is from the multiplicities of postscission light particles emitted from the fragments. For the symmetric window, we have used our data for postscission  $\alpha$  and proton emission, together with measurements of postscission neutron emission multiplicities for the system  $^{186}\text{Pt}$  from Hilscher *et al.* [23]. We have then added an estimate of the energy removed by  $\gamma$  decay, together with the  $Q$  value for emission (starting from an assumed scission nucleus which takes into account the estimated mass and charge removed prior to scission). In this way we have

determined the single fragment excitation energy after scission. The contributions to the resultant total value of 49.2 MeV are indicated in Table III. Adding the difference between the fission  $Q$  value and the fragment total kinetic energy calculated from Viola systematics [16], we obtain a total excitation energy at scission of 110 MeV for symmetric breakup. This result is slightly lower than that obtained in a previous study for  $A \approx 160$  [4]. Here, as in that work, symmetric breakup occurs near the end of the de-excitation chain.

##### C. Asymmetric breakup

Because we do not have neutron emission data for the asymmetric windows, we cannot employ the method used for symmetric fission to determine the excitation energies at scission for asymmetric fragmentations. To make such determinations, we used instead an empirical technique based upon some previous observations of charged particle emission in the deexcitation of medium mass nuclei [4,17,24,27].

In Fig. 12, the measured average multiplicities for (a)  $\alpha$  particles and (b) protons observed in coincidence with residues for systems with  $A_{\text{CN}} \sim 120$  and  $\sim 160$  are shown as a function of excitation energy per nucleon. Note that both the  $\alpha$  and the proton multiplicities increase linearly as the excitation energy per nucleon of the system increases,

$$\langle M \rangle = \kappa(E_x/A) - b. \quad (13)$$

From Figs. 12(a) and 12(b), we can see that the slope and intercept change with the mass of the system. To determine the excitation energies at scission for different fission fragment mass asymmetries in the  $^{136}\text{Xe} + ^{48}\text{Ti}$  reaction, we have assumed that the property of evaporated  $\alpha$  or proton multiplicity increasing linearly with the excitation energy per nucleon of the system is also valid for the present system with  $A_{\text{CN}} \sim 184$  and have established the slope  $\kappa$  in Eq. (13). From the measured precission  $\alpha$  and proton multiplicities observed for our system, we used the symmetric fission process to establish the slopes  $\kappa_\alpha$  and  $\kappa_p$ .

We proceeded as follows: From the deduced 98% linear momentum transfer for the symmetric fission channel as observed in Fig. 3, we estimate that the initial exci-

TABLE III. One fragment excitation energy at scission for symmetric fission.

Particle	$\langle M \rangle$	$\langle M \rangle \langle E \rangle$ (MeV)
$\alpha$	0.30	4.8
$p$	0.22	1.7
$n$	2.50	7.5
$\gamma$		(estimated) 6.0
Total kinetic energy (MeV)		20.0
Evaporation value $Q$ (MeV)		<u>29.2</u>
Excitation energy $E_x$ (MeV)		<u>49.2</u>

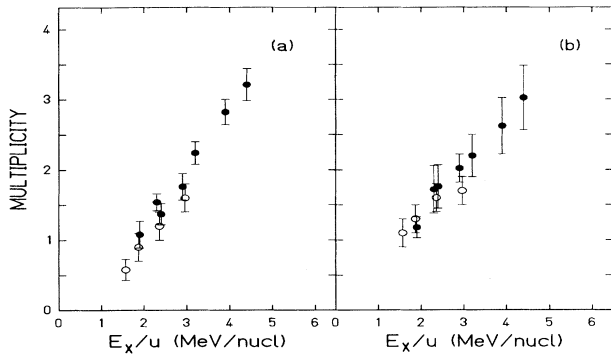


FIG. 12. (a)  $\alpha$  particle and (b) proton multiplicities as a function of excitation energy per nucleon. The solid dots with error bars represent the data for  $A_{CN} \sim 120$  from Ref. [17], and the open dots with error bars are the data for  $A_{CN} \sim 160$  from Ref. [24].

tation energy of the system is 570 MeV. The energy difference between the initial stage and scission stage for the symmetric fission process is then,  $570 - 110 = 460$  MeV. The observed precission  $\alpha$  multiplicity for symmetric fission is  $2.09 \pm 0.10$ . So the slope  $\kappa_\alpha$  determined for the composite system is  $0.834 \pm 0.040$ . In a similar way, we obtained the slope for proton emission from the composite system as  $0.976 \pm 0.040$ .

Assuming these slope parameters for  $\alpha$  and proton emission to be valid for all final fragment asymmetries, we can immediately transform the observed precission multiplicities into excitation energies at scission, i.e.,

$$E_{x(\text{sciss})} = E_{x(\text{init})} - \frac{A}{\kappa} \langle M \rangle_{\text{pre}}. \quad (14)$$

The scission excitation energies determined in this way appear in Table IV, columns 2 and 4. Note that the excitation energies determined from  $\alpha$  and protons are in good agreement. The uncertainties quoted represent the experimental errors on the measured multiplicities.

Although less accurate, it is also possible to apply the same basic technique to emission from the fragments if the intercept  $b$  of Eq. (13) is known. For example, for symmetric decay, the excitation energy of a fragment is 49.2 MeV. The estimated total precission emission for symmetric fission is 30 mass units which results in symmetric fragment masses at scission of 77 amu. The  $\alpha$  multiplicity for emission from the fragment is  $0.30 \pm 0.05$ . Using previous results of Wada *et al.* [17], Gonin *et al.* [4], and Viesti *et al.* [24], and assuming a linear variation of intercept  $b$  with  $A$ , we have established for  $\alpha$  particles

TABLE IV. Excitation energy at scission for different mass asymmetries.

$A_H/A_L$	$E_X$ (MeV) ( $\alpha_{\text{pre}}$ )	$E_X$ (MeV) ( $\alpha_{\text{post}}$ )	$E_X$ (MeV) ( $p_{\text{pre}}$ )	$E_X$ (MeV) ( $p_{\text{post}}$ )
1.00	$110 \pm 22$	$110 \pm 6$	$110 \pm 18$	$110 \pm 18$
1.56	$162 \pm 22$	$172 \pm 13$	$152 \pm 18$	$146 \pm 32$
2.54	$228 \pm 22$	$276 \pm 14$	$234 \pm 32$	$224 \pm 30$
4.75	$360 \pm 57$	$499 \pm 73$	$385 \pm 22$	$409 \pm 29$

a formula for the intercept as a function of mass  $A$ :

$$b_\alpha = 0.00588A - 0.235. \quad (15)$$

For protons, we take the intercept to be one-half of the  $\alpha$  intercept,

$$b_p = 0.5(0.00588A - 0.235). \quad (16)$$

Using these intercept formulas and assuming a linear variation of  $\kappa$  with  $A$ , we obtained the following slope formulas for our system as a function of mass  $A$  of the emitting nucleus:

$$\kappa_\alpha = 0.00024A + 0.79, \quad (17)$$

$$\kappa_p = 0.0043A + 0.18. \quad (18)$$

Using Eqs. (13)–(18), we have determined the excitation energy at the scission point for scission with different mass asymmetries from the postscission  $\alpha$  and proton multiplicities. Columns 3 and 5 in Table IV contain the results from that analysis. These are in reasonable agreement, within errors, with the same quantities derived from the precission particle emission.

These results are also plotted in Fig. 13 as a function of mass asymmetry. In that figure, we can easily see that for the very relaxed processes selected, scission occurs at an increasingly earlier stage of the deexcitation cascade as the mass asymmetry increases. The general trend of shorter lifetimes for asymmetric splits has been noted previously by several research groups [8–10].

#### D. The precission times

In order to extract the times for scission with different mass asymmetries, we employed results of EVAP, a modified version of the statistical model computer code PACE2 [25] to calculate the precission lifetime as a function of excitation energy. These calculations were carried

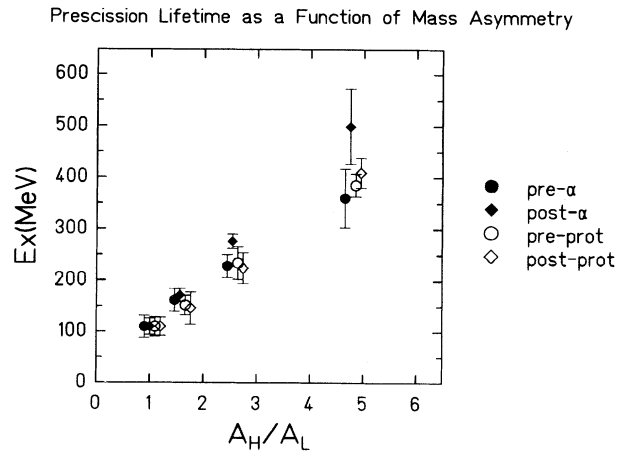


FIG. 13. The excitation energy at scission for different fission fragment mass asymmetries as deduced from the precission  $\alpha$  multiplicity ( $\bullet$ ), the postscission  $\alpha$  multiplicity ( $\circ$ ), the precission proton multiplicity ( $\diamond$ ), and the postscission proton multiplicity ( $\blacklozenge$ ). For clarity, some points are slightly displaced on the mass asymmetry scale.

out for us by N. Nicolis of Washington University. The decay by  $n$ ,  $p$ ,  $d$ ,  $\alpha$ ,  $t$ ,  ${}^3\text{He}$ , and  ${}^6\text{Li}$  has been considered in the calculation of decay widths. The statistical fission decay was suppressed in the calculation.

The precission lifetime can be determined by accumulating the light particle emission lifetime along the precission de-excitation chain:

$$\tau(E_x) = \sum_{E_x} \frac{E_x^0}{\Gamma_i} \hbar, \quad (19)$$

where  $\Gamma_i$  is the decay width of emitted light particles,  $E_x^0$  is the initial excitation energy of the system, and  $E_x$  is the excitation energy of the daughter after the  $i$ th particle is emitted. The level density  $\rho(E, J)$  used in these calculations is given by

$$\rho(E, J) = \rho_0(U) (2J + 1) \exp\{2\sqrt{a[U - E_{\text{rot}}(J)]}\}, \quad (20)$$

where “ $a$ ” is the level density parameter and  $U = E - \Delta$  where  $\Delta$  is the pairing energy.  $E_{\text{rot}}$  is the rotational energy and  $\rho_0(U)$  is taken from the Gilbert and Cameron formalism [26]. The calculated precission lifetimes are strongly influenced by the level density parameters “ $a$ .” In this work, we have made calculations for  $a = A/8$ ,  $A/10$ , and  $A/12$ .

Figure 14(a) shows the calculated lifetime as a function of the excitation energy in  ${}^{184}\text{Os}$  for different values of the level density parameter,  $a$ . Figure 14(b) shows the calculated cumulative decay time as a function of the excitation energy for different values of the level density parameter “ $a$ .” The dot-dashed lines correspond to times determined by assuming a level density parameter  $a = A/8$ ; the dashed lines correspond to the times determined by assuming a level density parameter  $a = A/12$ ; the solid line corresponds to the times determined by assuming a level density parameter  $a = A/10$ ; and the solid points on

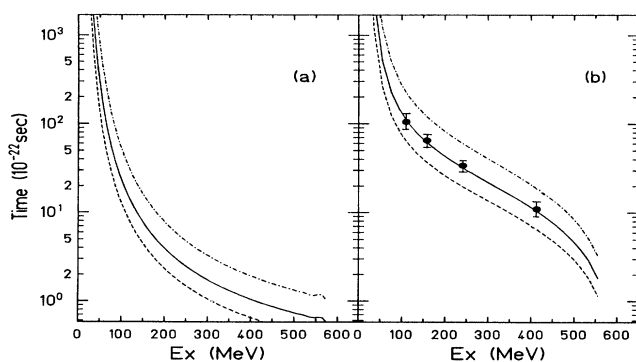


FIG. 14. (a) Lifetime as a function of the excitation energy for  ${}^{184}\text{Os}$  at the initial excitation energy of 560 MeV. (b) Cumulative decay time as a function of the excitation energy. The solid line results from the calculation assuming a level density parameter  $a = A/10$ ; the dot-dashed line from assuming  $a = A/8$  and the dashed line from assuming  $a = A/12$ . The solid dots with error bars indicate the precission times for the four mass asymmetry windows determined from the excitation energies at scission, and assuming  $a = A/10$  as a reasonable average value.

the solid line correspond to the excitation energies determined in the experiment. The time depends strongly on the level density parameter. Previous studies indicate that the inverse parameter  $K = A/a$  increases as the excitation energy per nucleon of the system increases [27–29]. Along the de-excitation path,  $K = A/a$  is expected to vary from  $\sim 14$  to 8.

In Fig. 15, we show the pre-scission times extracted from our experimental results by assuming  $a = A/10$  and also show pre-scission times obtained by assuming the empirically determined temperature dependent level density parameter which is presented in Ref. [28]. In this figure, two other times are shown. The diamond represents the symmetric fission times calculated by the Feldmeier model [30], which will be discussed in the following section. The star represents the symmetric fission time of  $8 \times 10^{-21}$  seconds obtained by Hilscher *et al.* for the  ${}^{186}\text{Pt}^*$  system using a neutron clock ( $a = A/10$ ) [23]. For a range of  $A_H/A_L$  of 1.6 to 8, Hilscher *et al.* also reported a precission time of  $\sim 3 \times 10^{-21}$  s for the  ${}^{186}\text{Pt}^*$  system [23].

Table V summarizes our results. In that table,  $E_x$  is excitation energy at scission,  $\tau(A/10)$  is the precission time obtained by assuming a level density parameter  $a = A/10$  and  $\tau(a(T))$  is the precission time obtained by assuming a temperature-dependent level density parameter. We note that these times are based on the assumption of sequential decay of an equilibrated system. As seen in Fig. 14, the calculated statistical lifetimes at excitation energies of 500 MeV become very short. This raises questions about the applicability of the calculation, as these times are shorter than typical times for nucleons to traverse the nucleus. As the lifetime increases exponentially with decreasing excitation energy, this has lit-

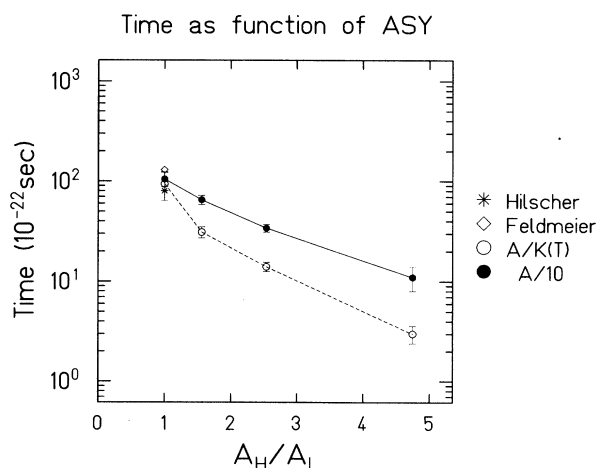


FIG. 15. Precission lifetime as a function of mass asymmetry. Solid symbols (●) represent the precission time scale extracted from our experiment assuming  $a = A/10$ . Open symbols (○) represent the precission time scale assuming a temperature-dependent level density parameter. (For clarity, points are slightly displaced on the mass asymmetry scale.) The lines are to guide the eye. Asterisk indicates the precission time scale obtained by Hilscher *et al.* for the system  ${}^{186}\text{Pt}^*$ , and (◇) indicates the precission time scale calculated using the Feldmeier model and assuming  $L = 120\hbar$ .

TABLE V. Excitation energies and scission times.

$A_H / A_L$	$E_x$ (MeV)	$\tau(A/10)$ ( $10^{-21}$ s)	$\tau(a(T))$ ( $10^{-21}$ s)
1.00	$110 \pm 9.4$	$10.5 \pm 0.7$	$9.4 \pm 3.0$
1.56	$158 \pm 11$	$6.5 \pm 0.7$	$3.1 \pm 0.4$
2.54	$241 \pm 13$	$3.4 \pm 0.3$	$1.4 \pm 0.1$
4.75	$413 \pm 25$	$1.1 \pm 0.3$	$0.3 \pm 0.06$

tle effect on the result expected for symmetric fission. A greater uncertainty results for the more asymmetric breakups.

## V. DISCUSSION

The times determined in our work are for the highest excitation energy events, selected on the basis of highest

total kinetic-energy loss. To learn about the extent to which deep inelastic collisions or compound nucleus evaporation may account for the observed scission times, we have explored the angular distributions of the fragments emitted in these reactions.

In the first column of Fig. 16, we present the fragment angular distributions  $d\sigma/d\theta$  observed in the center-of-mass frame for the different mass asymmetry windows in our experiment. In the second column are distributions calculated with our geometry filtered Monte Carlo simulation. The third column shows the data after a geometry correction determined from the Monte Carlo simulation is applied. In our Monte Carlo simulation, we assumed a constant  $d\sigma/d\theta$  initial distribution. After geometric corrections, we see that for symmetric fission (Asy1), the experimental fragment angular distribution  $d\sigma/d\theta$  is almost constant. For the Asy2, Asy3, and Asy4 windows, the fragment angular distributions show progressively in-

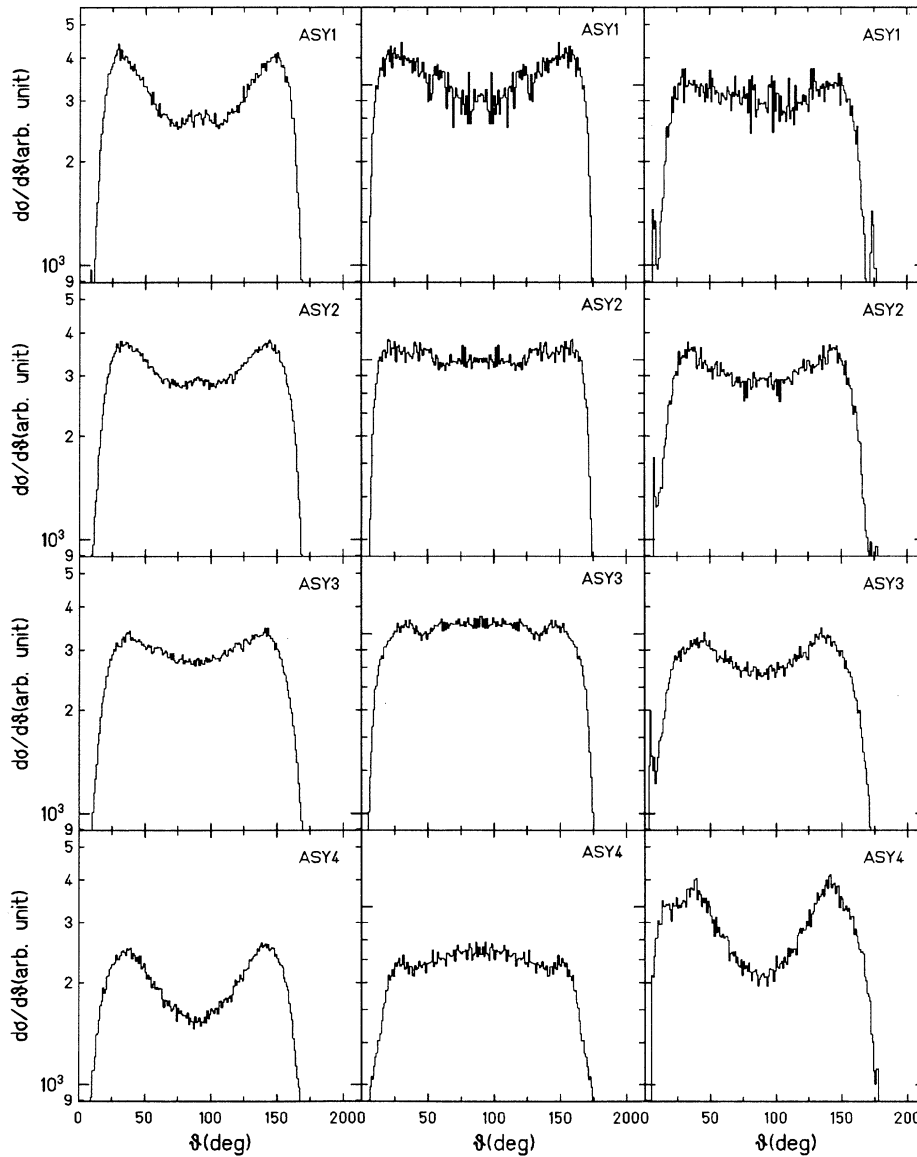


FIG. 16. The fragment angular distribution in the center-of-mass frame for different mass asymmetries. Experiment results (first column), Monte Carlo simulation assuming constant  $d\sigma/d\theta$  and filtering through the experimental geometry (second column), and geometry corrected data (third column).

creasing forward-backward peaking corresponding to noncompound processes with the heavier fragment emitted in the forward direction. These results indicate that even for the high total kinetic-energy loss processes, the asymmetric mass splits still include a significant fraction of events corresponding not to decay of a completely equilibrated compound nucleus, but rather to scission of a strongly damped dinucleus.

In order to better understand the role of dissipative phenomena in the binary decay processes which we have studied, we have made some calculations with the Feldmeier “one-body” dissipation model [30] which was developed to describe deep-inelastic collisions. Table VI shows the orbital angular momentum  $L$ , total kinetic energy loss (TKEL), lighter fragment mass  $A_L$ , and contact time  $\tau$ , calculated with the Feldmeier model for the system  $^{136}\text{Xe} + ^{48}\text{Ti}$  with incident energy 18.5 MeV/nucleon. These results show that as the angular momentum decreases, the calculated energy dissipation increases and the contact (pre-scission) times become longer.

In Fig. 17 we show, for several systems, empirical estimates of the impact parameter ratio ( $b/b_{\text{max}}$ ) as a function of the total kinetic-energy loss ratio ( $\text{TKEL}/\text{TKEL}_{\text{max}}$ ) obtained from cross section and  $\gamma$ -ray measurements [15]. For our system, the heavily damped events have  $\text{TKEL}/\text{TKEL}_{\text{max}} \approx 0.8$ , which indicates  $b/b_{\text{max}} \approx 0.4$ . Thus the orbital angular momentum is expected to be  $\leq 150\hbar$ . In the Feldmeier calculation for  $L = 120\hbar$ , the pre-scission time for the near symmetric breakup is  $1.25 \times 10^{-20}$  s, close to that of the experiments as see in Fig. 15. At this time, the energy dissipation is essentially complete.

For angular momenta higher than  $120\hbar$ , calculations indicate that the system does not reach a shape equilibration, but goes through a deep-inelastic process with energy dissipations which decrease as the mass asymmetry at scission increases. For angular momenta  $L < 90\hbar$ , the calculation indicates that the system forms a fused compound nucleus which does not scission in this calculation, but could deexcite by fission or fragment emission.

For the most asymmetric breakups observed in this work, the observed pre-scission lifetime is near  $1 \times 10^{-21}$  s. In the calculation, such short time events do not undergo the large energy dissipations seen for those events selected in our study. To provide such events in the calculation would require introduction of very large fluctuations in the energy dissipation and/or interaction time.

TABLE VI. Feldmeier model calculations.

$L$ ( $\hbar$ )	TKEL (MeV)	$A_L$ ( $u$ )	$\tau$ ( $10^{-22}$ s)
350	38	55	5.48
300	357	59	9.33
250	467	63	18.8
200	490	76	33.6
150	511	81	68.8
120	518	84	125.0
100	521	89	242.0
90	522	91	435.0

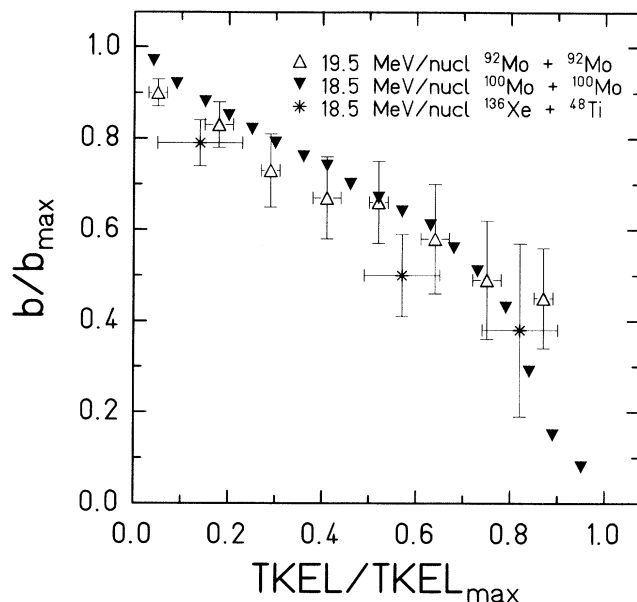


FIG. 17. The impact parameter ratio ( $b/b_{\text{max}}$ ) as a function of relative total kinetic-energy loss ( $\text{TKEL}/\text{TKEL}_{\text{max}}$ ) [15].

To further explore the time scales, we compared the  $\alpha$  energy spectra from which we obtained the pre-scission-postscission multiplicities with the  $\alpha$  energy spectra which are observed in coincidence with the fragments with the additional condition that the lighter fragment kinetic energy must be lower than 100 MeV in the center of mass. This condition excludes most of the events which lead to a forward-backward peaking much stronger than expected for the compound nucleus. We found no significant change in the coincident particle spectra, and hence no change in the times derived. Placing a window on events in which the light fragment goes forward and the heavy fragment backward in the center-of-mass frame leads to the same conclusion.

Without further information we cannot unambiguously determine the relative contributions of completely damped deep-inelastic and evaporation contributions to the fragment decays observed in the different mass asymmetry windows. However, we note that compound nucleus formation and decay processes may generally be expected to take longer than the deep-inelastic reactions leading to the same exit channel mass asymmetry. Thus, to the extent that the observed events do contain significant contributions from both processes, the times determined may be viewed as upper limits to the deep-inelastic separation times and lower limits to the compound nucleus decay times. In this latter case, the results indicate that there may be significant dynamic delays in the evaporation of fragments of  $A > 20$ . We emphasize this point in Fig. 18 by comparing our experimental mean excitation energies at scission with the corresponding mean excitation energies determined for statistical fragment emission using the code GEMINI [31]. Our results suggest that a realistic treatment of hot nucleus de-excitations will need to take into account dynamic restrictions over a wide range of fragment masses.

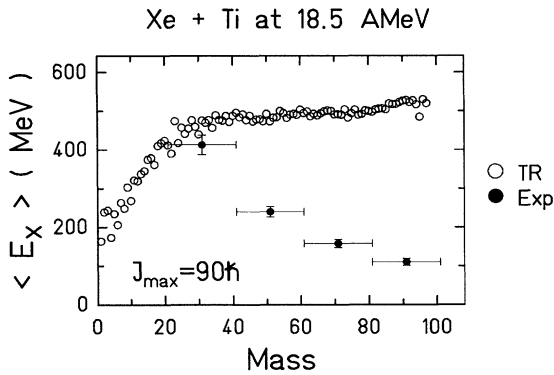


FIG. 18. Comparison between experimentally determined and calculated average excitation energies for fragment emission. The solid points represent the data. The open circles are the results of a calculation using the statistical model code GEMINI with a maximum angular momentum of  $90\hbar$ .

## VI. SUMMARY AND CONCLUSION

For the system  $^{136}\text{Xe} + ^{48}\text{Ti}$  at 18.5 MeV/nucleon, this research presents a systematic study of the precission time scales for relaxed processes as a function of fragment mass asymmetry. Fragment velocities were measured. The fragment masses were deduced by means of a kinematic reconstruction. The light charged particles emitted in coincidence with fragments were observed with good resolution in mass asymmetry. An empirical technique was used to obtain the excitation energy at scission from the multiplicities of the emitted light particles. From these energies, precission lifetimes were determined. From the experiment, we conclude that for very hot nuclei with  $A \sim 180$  having initial excitation energies about 3 MeV/nucleon, symmetric breakup still occurs at the very end of the de-excitation chain at an excitation energy around 110 MeV. Symmetrically fissioning nuclei are cold at scission. This is apparently because the time needed for the hot nucleus to change shape into two nearly equal sized nuclei is  $\sim 1 \times 10^{-20}$  s. During this time, the very rapid evaporation of light particles removes the extra excitation energy, leaving the system relatively cold.

For the highest excitation energy events, asymmetric breakups happen at an earlier stage of the particle de-excitation chain than the symmetric breakup. The greater the fragment mass asymmetry, the earlier in the de-excitation stage the scission occurs. For the most asymmetric breakup observed here, the time to scission is  $(0.3-1.1) \times 10^{-21}$  s. Some of the asymmetric mass-split processes might be correlated with higher angular momenta, reflecting large fluctuations in energy dissipation or interaction time in deep inelastic collisions.

Since the observed fragment emissions reflect a mixture of deep-inelastic and fusion-fission processes, we cannot unambiguously determine the lifetime for each independently from our data. We argue, however, that the data may provide an important indication that a fragment mass dependent variation of dynamic delay times in fragment evaporation may be an important effect which

needs to be taken into account in modeling the de-excitation of hot nuclei, even for relatively light fragments.

## ACKNOWLEDGMENTS

This work was supported by the U.S. Department of Energy under Grant No. DE-FG05-86ER40256, the Robert A. Welch Foundation, and the National Science Foundation. We thank N. Nicolis for providing statistical model calculations and H. Feldmeier for making his code available.

## APPENDIX

One technique to search for spurious contributions in the detected two-body events is to use the minimized quantity  $\Delta_v$ , the difference between the measured fragment velocity and the reconstructed primary fragment velocity [see Eq. (4)].

If the perturbations of the primary velocities follow a Gaussian distribution, then  $\Delta_v$ , being the sum of the squares of Gaussian random variables, should be distributed like a  $\chi^2$  function with two degrees of freedom. Figure 19 shows the  $\Delta_v$  distributions for the four mass asymmetry windows for the fully relaxed events considered in our analysis. The solid histograms correspond to all events giving a twofold coincidence in the detector (true binary events + incompletely measured events of higher multiplicity).

Olmi *et al.* [12] have interpreted the long tailing of the  $\Delta_v$  spectrum for the detected two-body events, which extends beyond the expected  $\chi$ -shaped distribution, as the background from higher multiplicity events. Casini *et al.* [13] proposed a method to estimate this background, and verified this method by a Monte Carlo simulation. The background was obtained from an analysis of measured three-body events by using the two-body kinematic reconstruction after having chosen at random two out of the three fragments. Following the reconstruction, they normalized this pseudo two-body  $\Delta_v$  distribution to the detected two-body  $\Delta_v$  distribution at high  $\Delta_v$  to estimate the background.

For our data, the dotted histograms in Fig. 19 represent the estimated background contribution which is obtained by applying two-body kinematics to the completely measured ternary events after two out of three fragments have been randomly chosen. If this method were appropriate, a 20% background of ternary events contributing to our measured twofold events would be indicated. In fact, the nature of the  $\Delta_v$  distribution will change significantly depending upon the mass of the missing third fragment. For symmetric fission events, this feature is demonstrated in Fig. 20 in which we show the effects of always excluding the lightest fragment of a three-body event [Fig. 20(a)], always excluding the medium mass fragment [Fig. 20(b)], or always excluding the heaviest fragment [Fig. 20(c)]. The heavier the fragment, the stronger the contribution to the high  $\Delta_v$  tail. Similar results are obtained for the other mass asymmetry windows.

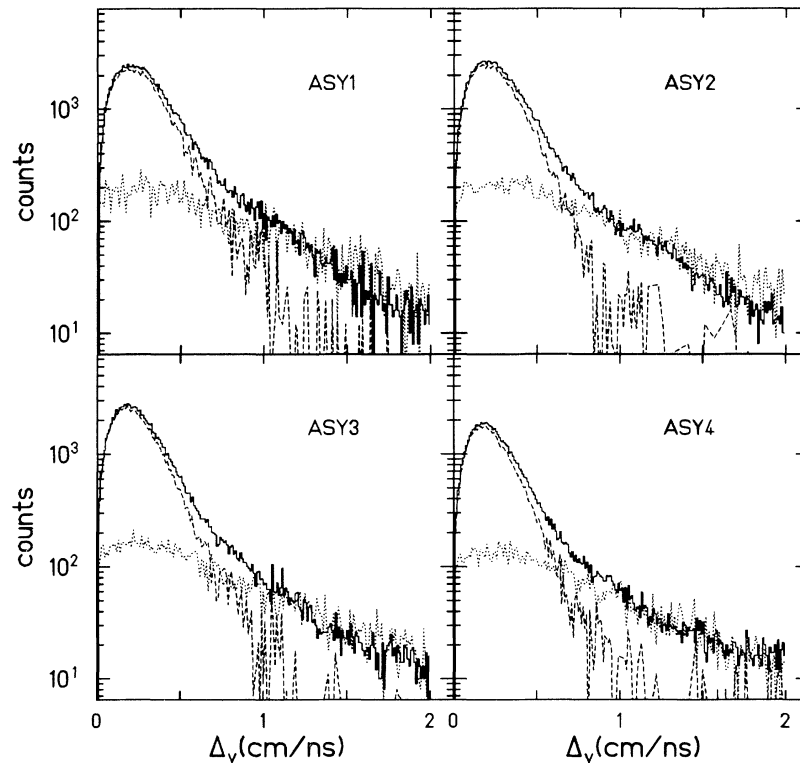


FIG. 19.  $\Delta_v$  distributions for the four mass asymmetry windows (see text). The solid histograms correspond to the twofold events, the dotted histograms represent the estimated background (obtained from the completely measured ternary events, with two-body kinematics after choosing two out of three fragments randomly), and the dashed histograms represent the  $\Delta_v$  distribution of twofold events corrected for the background of three-body events as determined by the method described in the text.

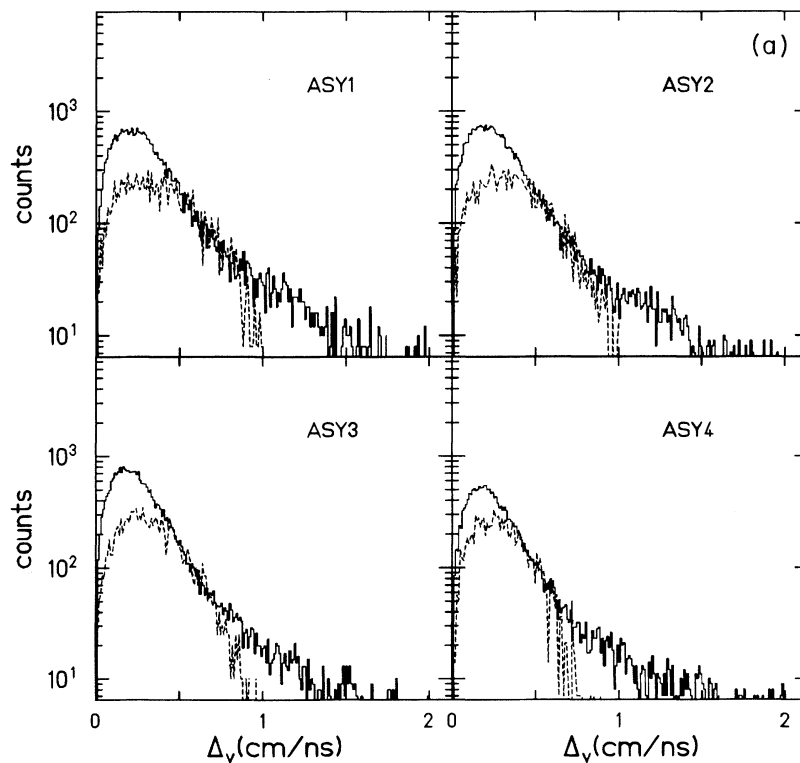


FIG. 20.  $\Delta_v$  distributions for the four asymmetry windows. The solid histograms correspond to the twofold events, the dotted histograms represent the estimated background obtained by excluding from a three-body event the lightest fragment (a), the medium mass fragment (b), and the heaviest fragment (c), and then using the remaining two fragments and two-body kinematics.

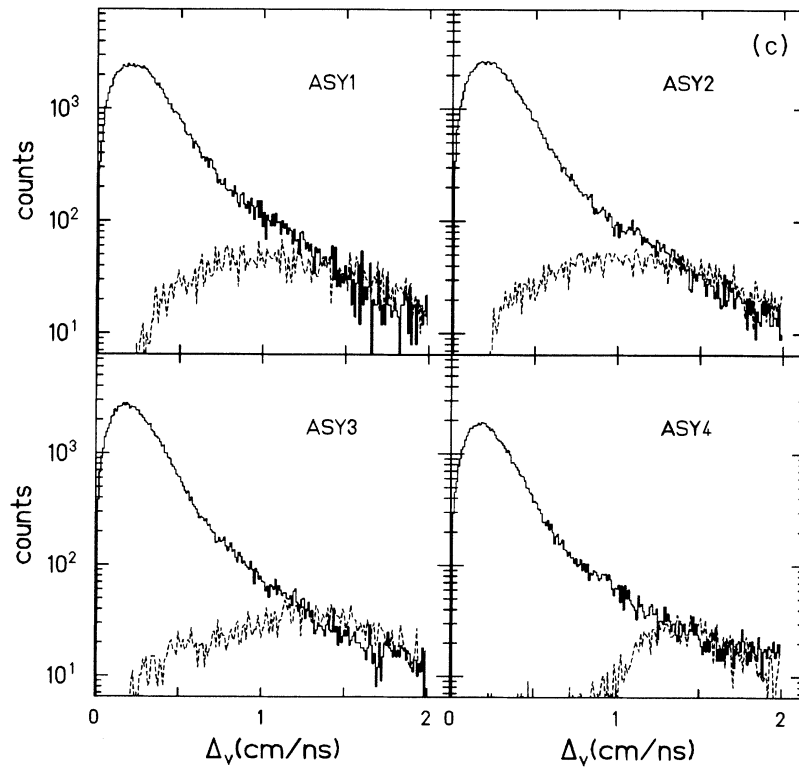
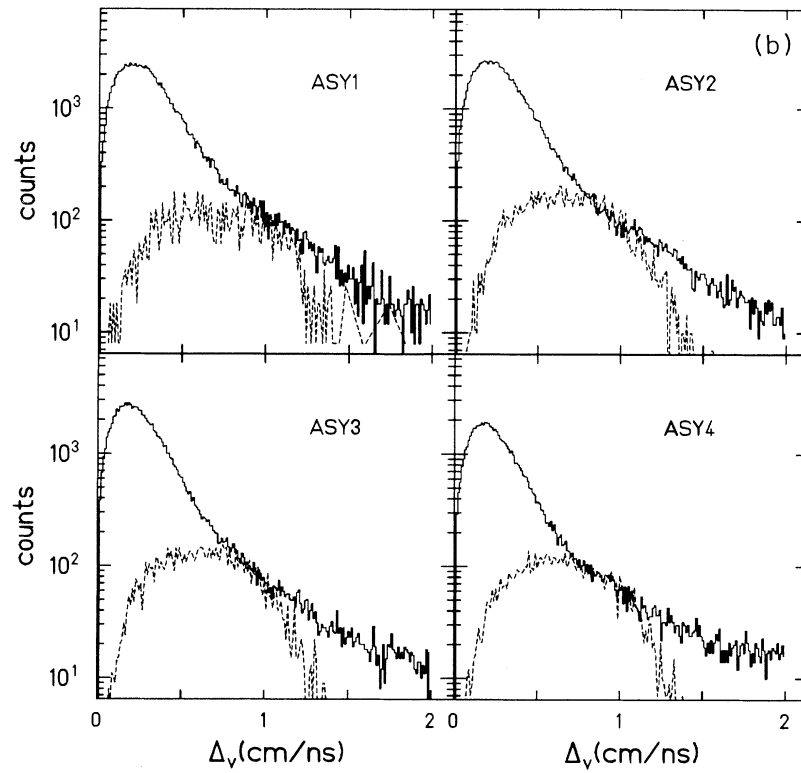


FIG. 20. (Continued).

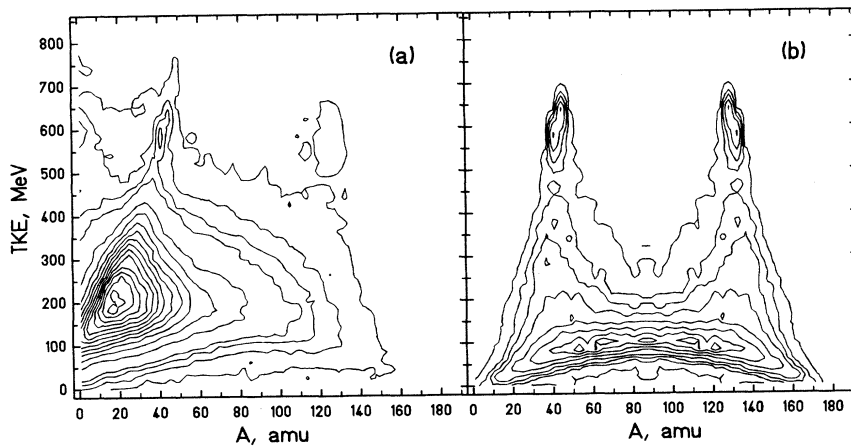


FIG. 21. The contour plot of the primary fragment masses vs total kinetic energy (TKE) for the three-body events (a) and for three-body events for which the lightest fragment has a mass  $15 \geq A \geq 5$  and this fragment is excluded in the kinematic analysis. For (a), the outermost contour is 10, then 50, 100, 150, and 200; then the contours increase linearly by increments of 200. For (b), the outermost contour is 10, then 30, 50, and 80; then the contour values increase linearly by increments of 50.

The PPAC detector efficiency decreases dramatically for  $Z \leq 10$ . As a result, we expect the probability for a lighter fragment to escape detection to be much higher than that for a heavier fragment. To explore this possibility, we present in Fig. 21 a contour plot of fragment mass versus total kinetic energy (TKE), for (a) the detected three-body events and (b) for those three-body events in which the lightest fragment, which has mass  $15 \geq A \geq 5$  is excluded from the kinematic reconstruction. In (a), we can see a peak in fragment mass around  $A \sim 20$ , reflecting the decrease of the detector efficiency at lower mass. Figure 21 also shows that for three-body

events, the peak of TKE is  $\sim 200$  MeV. From the contour plot obtained from detected two-body events (Fig. 2), we can see that total kinetic energy for events with  $A$  around 20 is below 100 MeV. A comparison of Fig. 2 to the contour plot obtained from pseudo-two-body events indicates that there might be a significant contribution to our data from apparent two-body events in which we have missed detection of one IMF. The difference in TKE for a three-body and pseudo-two-body events is consistent with the kinetic energy expected for such a missing IMF.

In order to better understand events for which a rela-

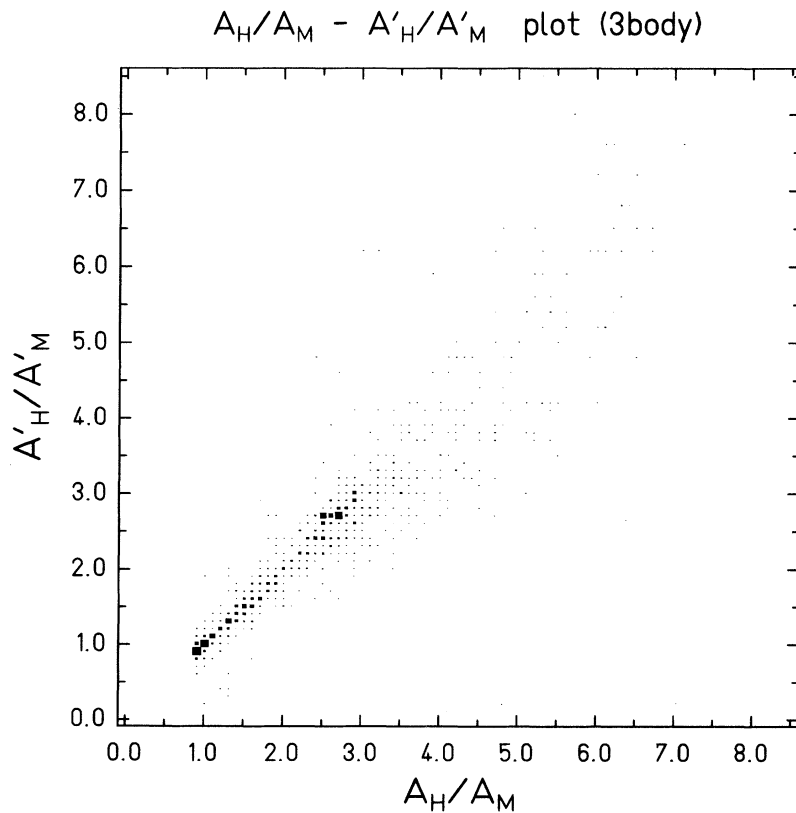


FIG. 22. Two-dimensional plot for mass ratio  $A_H/A_M$  of the two heavier fragments from detected three-body events vs the fragment mass ratio  $A'_H/A'_M$ , where  $A'_H$  and  $A'_M$  are the fragment masses determined by excluding the lightest fragment with  $5 \leq A \leq 15$ , and using the remaining two heavier fragments and two-body kinematics.

tively light IMF is missed, we have taken detected three-body events for which the lightest fragments have  $5 \leq A \leq 15$  and have, by excluding the lightest fragment from the analysis, done a two-body kinematic reconstruction with the two remaining fragments. We then compared the resultant  $\Delta_\nu$  distributions of these pseudo two-fold events with that of the measured twofold events. Normalizing the former to the latter indicates that about 65% of the events for the most asymmetric window (Asy4), and about 47% of the events in the other windows *could* result from events in which a light IMF is undetected.

To evaluate the effect of not detecting the IMF on our primary fragment mass and total kinetic energy determinations, we compared the reconstructed two fragment masses  $A'_1, A'_2$ , and the reconstructed total kinetic energy TKE'. For these pseudo-two-body events with the values obtained by analyzing the three-body event using all three fragments, Fig. 22 shows the two-dimensional plot of the original determined fragment mass ratio ( $A_H/A_M$ ), and the reconstructed two fragment mass ratio ( $A'_H/A'_M$ ). If we miss detection of one light fragment, the average reconstructed primary fragment

masses are miscalculated compared to the real primary fragment masses, but the fragment mass ratio for the remaining two fragments changes only slightly. A comparison of the original total kinetic energy (TKE) of the three-body events vs reconstructed pseudo two-body total kinetic energy (TKE') shows a linear relationship, but TKE' can be significantly lower than TKE, reflecting the energy removed by the excluded fragment.

### 1. Nature of detected three-body events

It is of interest to further characterize the three-body events which are detected. For the threefold events, Fig. 23 presents the angular distributions for fragments of different masses. The angular distributions of lighter fragments show backward peaking. Those of heavier fragments show forward peaking. These angular distributions imply a lot of peripheral, but strongly damped, collisions with projectilelike fragments going forward and targetlike fragments going backward in the center of mass. Fragments with masses  $A \sim 60$ , which could represent equal breakup into three pieces, have a nearly flat distribution in  $d\sigma/d\theta$ .

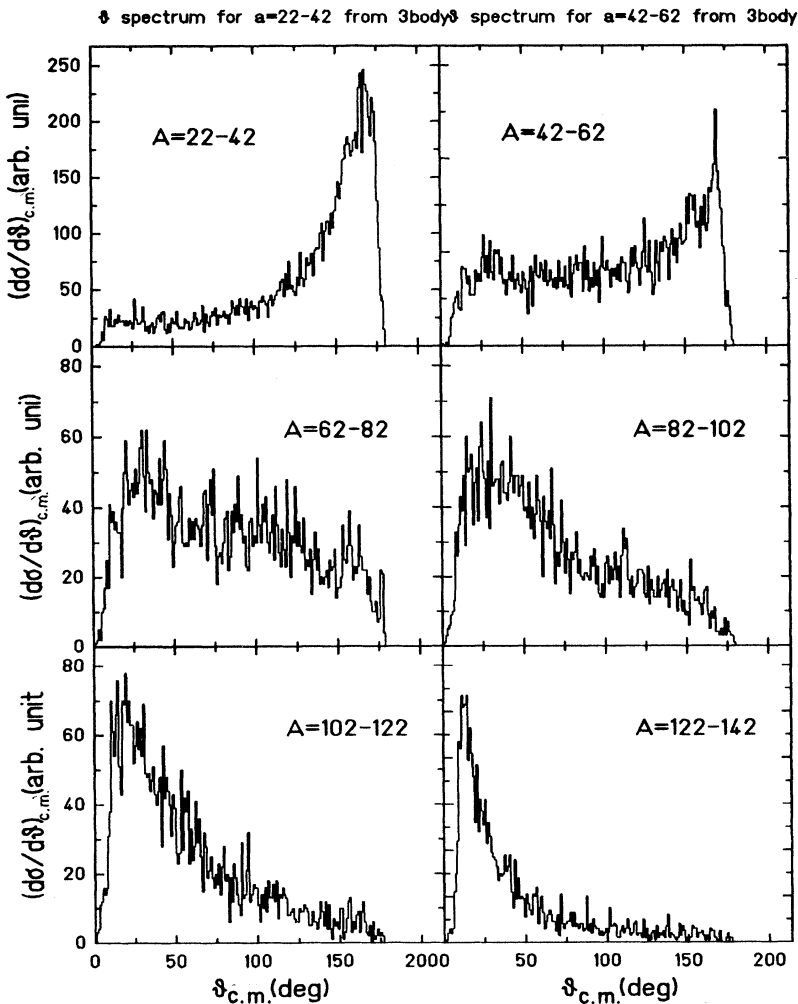


FIG. 23. The angular distribution,  $(d\sigma/d\theta)_{c.m.}$  for detected threefold events for the different fragment mass windows.

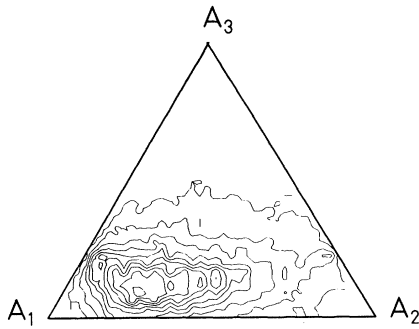


FIG. 24. Triangular contour plot of three-fragment masses for threefold events. The outermost contour is 10 events. The contours increase linearly by increments of 10.

In order to get a better understanding of these three-body events, we have looked at three fragment angular correlations and mass correlations. Figure 24 shows a triangular contour plot for the three fragment masses. In this plot, the three coordinates for the triangle diagram are the three fragment masses:  $A_1$ ,  $A_2$ , and  $A_3$ . We assumed the sum of the three fragment masses is  $A_{\text{tot}} = 184$ . The length of the perpendicular from any position inside the triangle to an edge represents the corresponding fragment mass. This figure shows a peak for  $A_1 \sim 120$ ,  $A_2 \sim 45$ ,  $A_3 \sim 20$ , which suggests some memory of the entrance channel for three-body events. Note that this plot is not symmetric because the indices are not randomly chosen. For each event, the index 1 is assigned to the fragment detected in the lowest numbered PPAC, 2 is assigned to the fragment detected in the next lowest numbered PPAC, and 3 to the fragment detected in the highest numbered PPAC. From the numbering system of the PPAC's, lower numbered PPAC's are at smaller angles, thus  $A_1$  is at a small angle.

Figure 25 shows a triangular contour plot of the angles between the fragments in the center-of-mass frame. In this plot, the three coordinates for the triangle diagram are the angles  $\theta_{\text{HM}}$  (the angle between the fragment with the heaviest mass and that with the next highest mass),  $\theta_{\text{HL}}$  (the angle between the fragment with the heaviest mass and the fragment with the lightest mass), and  $\theta_{\text{ML}}$

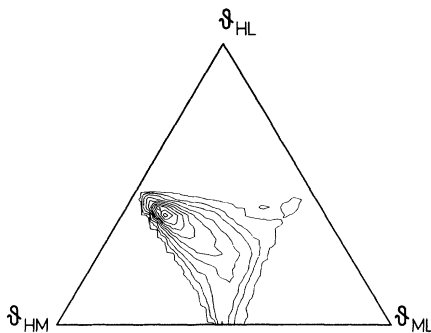


FIG. 25. Triangular contour plot of the folding angle between three fragments for detected threefold events. The outermost contour is 10, next is 50, then the contours increase linearly by increments of 100. See text for detail.

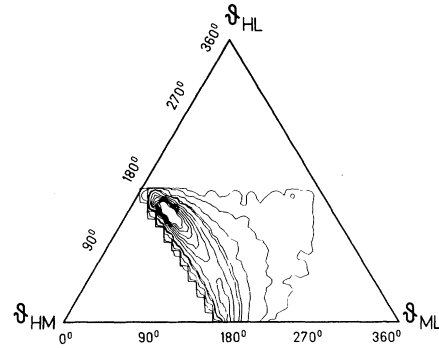


FIG. 26. Triangular contour plot of the folding angle between three fragments for threefold events with a very light fragment ( $5 \leq A \leq 15$ ). The outermost contour is 2, next are 10, 50, and 150; then the contours increase linearly by increments of 200.

(the angle between the middle mass fragment and the fragment with the lightest mass). The sum of these angles is  $360^\circ$ . The length of the perpendicular from any position inside the triangle to an edge represents the corresponding angle. This figure shows that in most of the three-body events, the folding angle between the lightest fragment and the middle mass fragment,  $\theta_{\text{LM}}$ , is relatively small, while the angles  $\theta_{\text{HM}}$  and  $\theta_{\text{LH}}$  are usually larger, approaching  $180^\circ$ . Figures 23–25 imply that in most of the detected three-body events, there is one larger fragment going forward while the two smaller fragments go backward. The majority of the detected threefold events appear to result from strong, projectile-target interactions in which a large energy dissipation and some transfer of mass from projectile to target is followed by fission of the target-like nucleus into two pieces, both of which go backward in the center-of-mass frame.

If we select detected three-body events with one very light fragment ( $5 \leq A \leq 15$ ) and construct the same type of figure (Fig. 26), we can see that the correlation between the medium mass and light mass fragment directions is reduced. Heavy mass and medium mass fragments are emitted essentially back-to-back, but the light fragment angle is distributed more uniformly. We believe this reflects the increasing importance of early IMF emission for the events selected in this way. To estimate the multiplicity of such intermediate mass fragments, we used the PPAC intrinsic efficiency given by Wessels [14] and the geometric efficiency determined by our Monte Carlo simulation (73%) to correct the data. We estimated the multiplicity of  $5 \leq A \leq 15$  fragments by using the detected three-body events, counting IMF's  $5 \leq A \leq 15$  detected by the PPAC's, correcting for the net detector efficiency, and normalizing to the total number of events. Using this method, we find a multiplicity  $\langle M_{\text{IMF}} \rangle \sim 1$  for  $5 \leq A \leq 15$ , a value which is similar to those reported for similar systems at comparable excitation energies.

From the observed three fragment mass and angular correlations, the majority of the detected three-body events appear to proceed via a deep-inelastic interaction followed by a sequential fission. Similar phenomena have been noticed by other groups [22].

- [1] J. M. Alexander, D. Guerreau, and L. C. Vaz, *Z. Phys. A* **307**, 149 (1983).
- [2] D. Hilscher, H. Rossner, B. Cramer, B. Gebauer, U. Jahnke, M. Lehmann, E. Schwinn, M. Wilpert, Th. Wilpert, H. Froeben, E. Mordhorst, and W. Scobel, *Phys. Rev. Lett.* **62**, 1099 (1989).
- [3] D. J. Hinde, H. Ogata, M. Tanaka, T. Shimoda, N. Takahashi, A. Shimohara, S. Wakamata, K. Katori, and N. Okamura, *Phys. Rev. C* **37**, 2923 (1988).
- [4] M. Gonin, L. Cooke, K. Hagel, Y. Lou, J. P. Natowitz, R. P. Schmitt, S. Shlomo, B. Srivastava, W. Turmel, H. Utsunomiya, R. Wada, G. Narelli, G. Nebbia, G. Viesti, R. Zanon, B. Fornal, G. Prete, K. Niita, S. Hannuschke, P. Gonthier, and B. Wilkins, *Phys. Rev. C* **42**, 2125 (1990).
- [5] M. Gonin, L. Cooke, B. Fornal, P. Gonthier, M. Gui, Y. Lou, J. B. Natowitz, G. Nardelli, G. Nebbia, G. Prete, R. P. Schmitt, B. Srivastava, W. Turmel, D. Utley, H. Utsunomiya, G. Viesti, R. Wada, B. Wilkins, and R. Zanon, *Nucl. Phys. A* **495**, 139c (1989).
- [6] F. P. Hessberger, V. Ninov, and U. Spoerel, *Z. Phys. A* **340**, 171 (1991).
- [7] S. Beiersdorf, R. A. Esterlund, M. Knaack, W. Westmeier, P. Patzelt, F. P. Hessberger, V. Ninov, and A. Lutgen, *Phys. Lett. B* **286**, 225 (1992).
- [8] G. F. Peaslee, N. N. Ajitanand, J. M. Alexander, D. Guerreau, R. Lacey, L. C. Vaz, M. Kaplan, M. Kildir, D. J. Moses, D. Logan, and M. S. Zisman, *Phys. Rev. C* **38**, 1730 (1988).
- [9] D. Hilscher, D. J. Hinde, and H. Rossner, in *Proceedings of the Texas A&M Symposium on Hot Nuclei*, edited by S. Shlomo, R. P. Schmitt, and J. B. Natowitz (World Scientific, Singapore, 1987).
- [10] D. J. Hinde, D. Hilscher, H. Rossner, B. Gebauer, M. Lehmann, and M. Wilpert, *Phys. Rev. C* **45**, 1229 (1992).
- [11] H. Stelzer, *Nucl. Instrum. Methods* **133**, 409 (1976).
- [12] A. Olmi, P. R. Maurenzig, A. A. Stefanini, J. Albinski, A. Gobbi, S. Gralla, N. Herrmann, K. D. Hildenbrand, J. Kuzminski, W. F. Muller, M. Petrovici, H. Stelzer, and J. Toke, *Europhys. Lett.* **4**, 1121 (1987).
- [13] G. Casini, P. R. Maurenzig, A. Olmi, and A. A. Stefanini, *Nucl. Instrum. Methods A* **277**, 445 (1989).
- [14] J. P. Wessels, Report No. GSI-90-21, ISSN 0171-4546 (1990).
- [15] E. Enders, Report No. GSI-91-15, ISSN 0171-4546 (1991).
- [16] V. E. Viola, K. Kwiatkowski, and M. Walker, *Phys. Rev. C* **31**, 1550 (1985).
- [17] R. Wada, D. Fabris, K. Hagel, G. Nebbia, Y. Lou, M. Gonin, J. P. Natowitz, R. Billerey, B. Cheynis, A. Demeyer, D. Drain, D. Guinet, C. Pastor, L. Vagneron, K. Zaid, J. Alarja, A. Giorni, D. Heuer, C. Morand, B. Viano, C. Mazur, C. Ngô, S. Leray, R. Lucas, M. Ribrad, and E. Tomasi, *Phys. Rev. C* **39**, 497 (1989).
- [18] E. Duek, N. N. Ajitanand, J. M. Alexander, D. Logan, M. Kildir, L. Kowalski, L. C. Vaz, D. Guerreau, M. S. Zisman, M. Kaplan, and D. J. Moses, *Z. Phys. A* **317**, 83 (1984).
- [19] B. Lindl, A. Brucker, M. Bantel, H. Ho, R. Muffler, L. Schad, M. G. Trauth, and J. P. Wurm, *Z. Phys. A* **328**, 85 (1987).
- [20] A. Brucker, B. Lindl, M. Bantel, H. Ho, R. Muffler, L. Schad, M. G. Trauth, and J. P. Wurm, *Phys. Lett. B* **186**, 20 (1987).
- [21] J. B. Natowitz, M. Gonin, K. Hagel, R. Wada, S. Shlomo, X. Bin, M. Gui, Y. Lou, D. Utley, T. Botting, R. K. Choudhury, L. Cooke, B. Hurst, D. O'Kelly, R. P. Schmitt, W. Turmel, H. Utsunomiya, G. Nebbia, D. Fabris, J. A. Ruiz, G. Nardelli, M. Poggi, R. Zanon, G. Viesti, R. H. Burch, F. Gramegna, G. Prete, D. Drain, B. Chambon, B. Cheynis, D. Guinet, X. C. Hu, A. Demeyer, C. Pasteur, A. Giorni, A. Lleres, P. Stassi, B. Viano, A. Menchaca-Rocha, M. B. Brandan, and P. Gonthier, *Nucl. Phys. A* **538**, 263c (1992).
- [22] R. J. Charity, R. Freifelder, A. Gobbi, N. Herrmann, K. D. Hildenbrand, F. Rami, H. Stelzer, J. P. Wessels, G. Casini, P. Maurenzig, A. Olmi, A. A. Stefanini, J. Galin, D. Guerreau, U. Jahnke, A. Peghaire, M. Gnirs, and D. Pelte, *Z. Phys. A* **341**, 53 (1991).
- [23] D. Hilscher, H. Rossner, B. Cramer, B. Gebauer, U. Jahnke, M. Lehmann, E. Schwinn, M. Wilpert, and Th. Wilpert, *Phys. Rev. Lett.* **62**, 1099 (1989).
- [24] G. Viesti, D. Fabris, G. Nebbia, G. Prete, K. Hagel, J. B. Natowitz, and R. Wada, in *Proceedings of the First Joint Italian-Japanese Meeting on Perspectives in Heavy Ion Physics*, Catania, Italy, 1992, edited by M. DiToro and E. Migneo (Italian Physical Society, Bologna, Italy, 1993).
- [25] A. Gavron, *Phys. Rev. C* **21**, 230 (1980).
- [26] A. Gilbert and A. G. W. Cameron, *Can. J. Phys.* **43**, 1446 (1965).
- [27] K. Hagel, D. Fabris, P. Gonthier, H. Ho, Y. Lou, Z. Majka, G. Mouchaty, M. N. Namboodiri, J. B. Natowitz, G. Nebbia, R. P. Schmitt, G. Viesti, R. Wada, and B. Wilkins, *Nucl. Phys. A* **486**, 429 (1988).
- [28] S. Shlomo and J. B. Natowitz, *Phys. Lett. B* **252**, 1987 (1990).
- [29] S. Shlomo and J. B. Natowitz, *Phys. Rev. C* **44**, 2878 (1991).
- [30] H. Feldmeier, *Rep. Prog. Phys.* **50**, 915 (1987); S. Chandrasekhar, *Rev. Mod. Phys.* **15**, 1 (1943).
- [31] R. J. Charity, M. A. McMahan, G. J. Wozniak, R. J. McDonald, L. G. Moretto, D. G. Sarantites, L. G. Sobotka, G. Guarino, A. Pantaleo, L. Fiore, A. Gobbi, and K. D. Hildenbrand, *Nucl. Phys. A* **483**, 371 (1988).